IMAGE CORRECTION FOR SOFT X-RAY PROJECTION MICROSCOPY

軟X線拡大投影顕微鏡による像修正に関する研究

January 2017

ERDENETOGTOKH JAMSRANJAV

Graduate School of
Advanced Integration Science
CHIBA UNIVERSITY

（千葉大学審査学位論文）

IMAGE CORRECTION FOR SOFT X-RAY PROJECTION MICROSCOPY

January 2017

軟X線拡大投影顕微鏡による像修正に関する研究

ERDENETOGTOKH JAMSRANJAV

Graduate School of
Advanced Integration Science
CHIBA UNIVERSITY

ABSTRACT

Soft X-ray microscopy has been developed for high resolution imaging of hydrated biological specimens due to the availability of water window region. In particular, a projection type microscope has a number of advantages in wide viewing area, easy zooming function and easy extensibility to CT (Computed Tomography). The blur of projection image due to the diffraction of X-rays, which eventually reduces spatial resolution, could be corrected by an iteration procedure, i.e., repetition of Fourier and inverse Fourier transformations. However, it was found that the correction is not sufficiently effective for all images. In this study, we first examined the iteration effectiveness by using images of latex particles and chromosomes with various magnifications. The results showed that iteration was not effective for the images with low contrast such as those of chromosomes. Then, we attempted to apply a contrast enhancement method to those same images to make diffraction fringes and specimen images clearer prior to the iteration procedure. The method was effective to improve the images uncorrectable solely by iteration procedure, and some chromosome images with low magnifications (Magnification: 47 ~ 219 times) and relatively high contrast were successfully corrected. The results of comparison for grayscale distributions between both correctable and uncorrectable images of latex particles and those of chromosomes showed that the background noise also may influence the iteration effectiveness. The background noise was apparently high for the chromosome images. Thus, we tried a noise removal method in combination with the contrast enhancement method as a next step. As a result, the chromosome images with magnification of 47 ~ 329 times were successfully corrected. However, the chromosome images with higher magnification remained at uncorrectable. Therefore, for further improvement of the effectiveness of image correction by computer processing, we evaluated the influence of the background noise in the iteration procedure through a simulation study. In this simulation study, images of the model specimen with known morphology instead of the chromosome images with very low contrast or relatively high contrast were used. Under the condition that artificial noise was distributed on the images randomly, we have introduced two different parameters to evaluate the noise effects with respect to each situation where the iteration procedure was not successful, and proposed an upper limit for the noise within which the effective iteration procedure for the chromosome images was possible.

TABLE OF CONTENTS

iii

LIST OF TABLES

LIST OF FIGURES

LIST OF ABBREVIATION

CCD   : Charge Coupled Device
CT   : Computed Tomography
FIB   : Focused Ion Beam
FFT   : Fast Fourier Transformation
FT   : Fourier Transformation
FZP   : Fresnel Zone-Plate
IFT   : Inverse Fourier Transformation
KAST   : Kanagawa Academy of Science and Technology
KEK   : High Energy Accelerator Research Organization
MSE   : Mean Squared Error
PF   : Photon Factory
RC-1   : Restraint condition for sampling number and intervals
RC-2   : Restraint condition for X-ray amplitude distribution on
                       specimen surface
RF   : Radio Frequency
VLS-PG   : Varied-Line-Spacing Plane Grating

ACKNOWLEDGEMENTS

CHAPTER 1: INTRODUCTION

1.1. BACKGROUND AND PURPOSE

There is strong demand of intact and/or in-situ observation of biological specimens at cellular and sub-cellular levels, especially in medical and biological fields [1-4]. X-ray microscopy has been highly anticipated to be the most suitable method to solve the above issue at hand. The X-ray's wavelength is shorter than that of the visible light. Therefore, imaging availability with high resolution is also expected for the X-ray microscopy [5].

Soft X-rays with wavelengths of 2.34-4.38 nm cover a special wavelength region called the "water window", where the X-ray absorption by water is significantly smaller than that by organic materials. This enables us to observe the biological specimens in a hydrated condition [6-8]. Imaging with smaller radiation damage is also possible for the biological specimens compared with electron microscopy [9, 10].

The history of the X-ray microscopy started when Wilhelm Roentgen discovered X-rays in 1895 and it has been developed for more than a hundred years [5, 11]. However, its resolution has not yet reached the level of the optical microscopy, mainly due to the fact that X-rays do not reflect or refract easily, unlike the visible light. Recent development in contact, scanning and imaging microscopes using soft X-rays has enabled high spatial resolution imaging at the scale of a few tens of nanometer, and also three dimensional imaging of hydrated biological specimens with cryo-CT system [12-17]. However those types of microscopes except contact microscopy have relatively complex optical layouts. On the other hand, the projection type microscopy is composed of a simple optical layout and has advantages over other types of microscopy particularly for the observation of biological specimens because of its wide viewing area, easy zooming function and easy extensibility to CT [18]. The projection type of X-ray microscopy was originally described by V. E. Cosslett and W. C. Nixon in 1951, first [5, 19]. As a result of its development about half hundred years, its resolution has been just achieved to about 100 nm [20].

This study aims to develop a soft X-ray projection microscopy which is applicable for the intact and/or in situ observation of biological specimens at its cellular and molecular levels. However, the image captured by the soft X-ray projection microscopy

is blurred by the diffraction of soft X-rays, resulting in the deterioration of spatial resolution. In our earlier studies, the blur was corrected by an iteration procedure, i.e., repetition of Fresnel and inverse Fresnel transformations [21-24]. However, the results showed that the correction was not necessarily effective for all images. Therefore recent studies have been focused on the cause of the ineffective correction and improvement of the correction effectiveness. Thus, this study addresses the following two issues.

(1) To investigate on the cause of the ineffective correction and to propose useful methods for image projection that would make the images correctable by the iteration procedure.

(2) To develop the image correction method that would also be effective in images even if there is a factor of ineffective correction.

In the beginning of this study, effectiveness of the correction by the iteration procedure was examined on projection images of chromosome and latex particles with 2 and 10 μm diameters in various magnifications. From the comparison of the successful corrected case with the insufficient corrected case, the cause of the insufficient correction was considered. From this examination, we recognized that the ineffective correction was mainly caused by the low image contrast and high background noises on the images. Therefore we applied an image improvement method consisting noise removal and contrast enhancement methods prior to the iteration procedure. As a result, some of images which were not correctable by the iteration procedure only, were corrected successfully after the image improvement. However the correction was not fully satisfied for the images with very low contrast and with high background noise. For consideration of further improvement of the correction effectiveness, we evaluated the upper limits of the background noise in which the image is effectively corrected in a simulation study. Based on results obtained in this study, the background noise on projection images can be evaluated during experiments and the optimization of the projection conditions by considering the upper limit of the noise is expected.

1.2. THESIS ORGANIZATION: A GUIDE THROUGH THE CHAPTERS

This thesis consists of six chapters. The first chapter introduces the background and purpose of this study.

The second chapter explains the general principles and theories for the soft X-ray projection microscopy. Electron storage ring was used as a soft X-ray source in this study. Therefore the electron storage ring and a general mechanism to generate synchrotron radiations (X-rays) are introduced in the beginning of the section (Section 2.1), followed by a description of the properties of soft X-rays particularly focusing on the water window region as an imaging principle of hydrated biological specimens (Section 2.2). In our soft X-ray projection microscopy system, Fresnel diffraction of soft X-rays is apparently produced, because monochromatic X-rays are applied. Principle and theory of the Fresnel diffraction are introduced in Section 2.3. A Fresnel zone plate was used in order to focus the X-ray beam to a point. Section 2.4 describes the Fresnel zone plate. Projection images are blurred by Fresnel diffractions. For the blur correction, calculations of the X-ray propagation and its inverse propagation were performed by Fourier (FT) and inverse Fourier transformations (IFT). Section 2.5 explains the FT and IFT.

In the third chapter, the instrument of the projection microscopy is introduced. In the instrument, BL-11A beamline of Photon Factory (PF) of High Energy Accelerator Research Organization (KEK), Tsukuba, Japan was used as a soft X-ray source. The PF electron storage ring and the BL-11A beamline are explained in section 3.1. Our projection microscopy system, which consists of a zone plate, a pinhole and a CCD (Charge Coupled Device) camera, is installed to the beamline. Section 3.2 describes details of the system.

Materials and methods of this study are described in the fourth chapter. In the first subsection (Section 4.1), projection method and conditions are described in detail. Subsequently, preparations of the specimens of chromosome and latex particle are presented in section 4.2. The details of iteration procedure and image improvement methods are explained in Section 4.3 and 4.4, respectively. In the last subsection (Section 4.5), a simulation and its correction procedure for the projection image of chromosomes is described.

In the fifth chapter, results and discussions of this study are presented. This study was performed in three steps that involved evaluations of the effectiveness of iteration procedure, effectiveness of the image improvement method and determination of the

upper limit of background noise on projection images which were corrected effectively. They are presented in subsections of 5.1, 5.2 and 5.3, respectively.

Finally conclusions obtained from the study are explained and the results and achievements in this study are outlined as a summary.

CHAPTER 2: PRINCIPLE AND THEORY

2.1. SYNCHROTRON RADIATION AND ELECTRON STORAGE RING

In this study, synchrotron radiation from electron storage ring was used as a soft X-ray source. The theoretical basis and the principles of the synchrotron radiation and the electron storage ring are introduced in this section.

The synchrotron radiation is produced when charged particles moving at the speed close to that of light change their direction by the effect of the magnetic fields in the electron storage ring. When an electron moves with a speed $\vec{v}$ in a magnetic field $\vec{B}$, it is effected by a magnetic force $\vec{F}$ defined as equation (2.1) from Lorentz force law [25].

$$\vec{F} = q\vec{v} \times \vec{B} \quad (2.1)$$

$\vec{F}$: Magnetic force to electron beam
q: Charge of electron beam
$\vec{v}$: Speed of electron beam
$\vec{B}$: Magnetic field

Direction of force can be found according to the right hand rule [26]. In this rule, you should hold your index finger, middle finger and thumb finger of your right hand at a position of perpendicular to each other, and index finger and middle finger should be held in parallel position to the speed of electron and magnetic field, respectively. Then the thumb finger points to the direction of the magnetic force.

Some kinds of magnetic and electric devices are installed in the electron storage ring for the purposes such as production of synchrotron radiation, electron acceleration for its energy loss and guidance of the electron beam to their reference path. A schematic diagram of the electron storage ring is shown in Fig. 2.1.
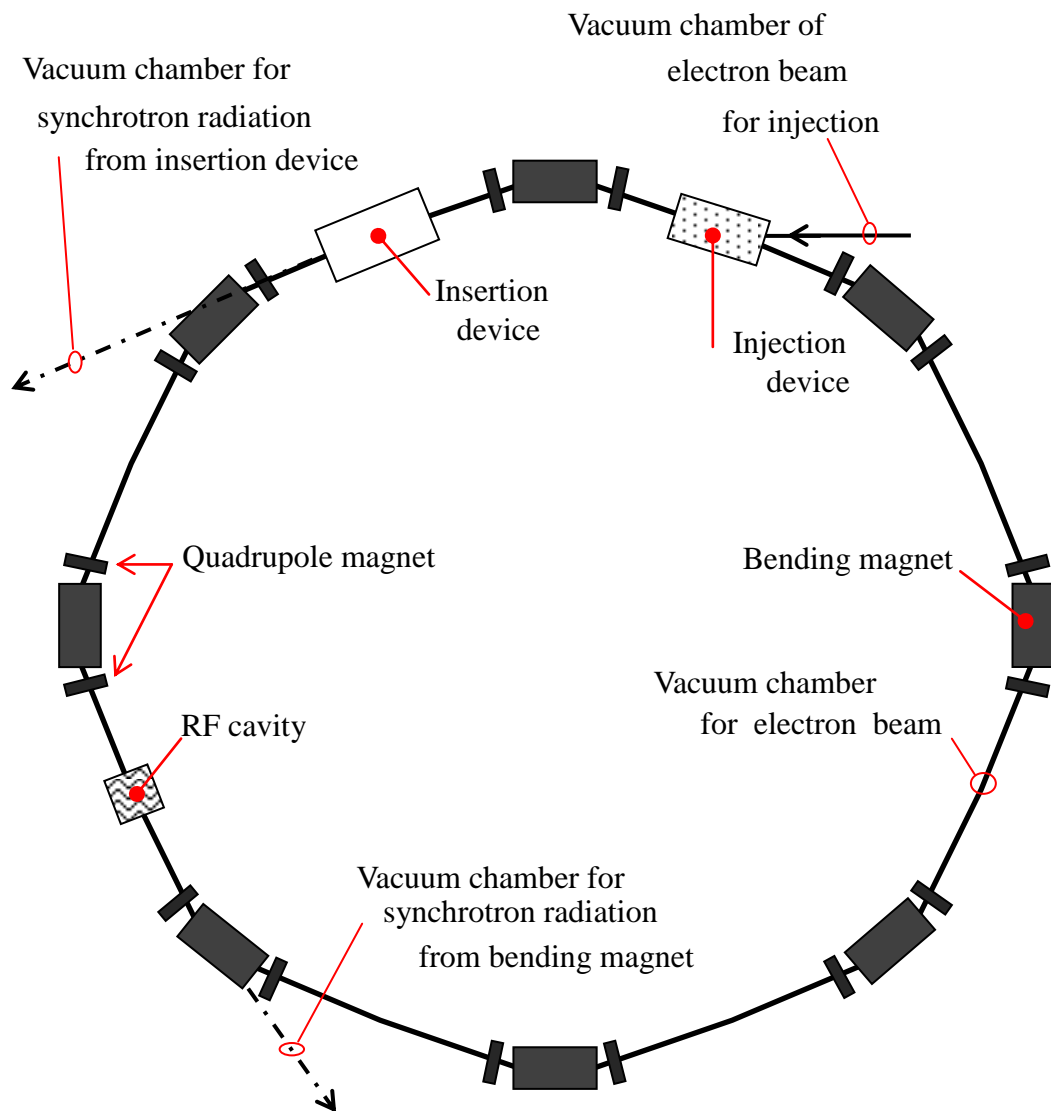
Fig. 2.1: Schematic diagram of the electron storage ring.

The electron storage ring consists of four types of magnetic devices called injection device, insertion device, bending magnet and quadrupole magnet, and an electric device called radio frequency cavity (RF cavity). The bending and quadrupole magnets are shown as large and small black squares. The insertion device, injection device and RF cavity are shown as a white square and squares filled with black points and waves, respectively. This figure also describes the process of producing synchrotron radiation, injection of electron beam to the storage ring and guidance of the electron beam to its reference path in the storage ring by magnetic devices. The details of those magnetic and electric devices will be explained in the next subsections (2.1.1 ~ 2.1.5).

The synchrotron radiation has the properties represented below [27, 28]. And it gives the possibility for users to select photons with special properties appropriate to their experiments.

(1) Broad and continuous spectrum from infrared to X-rays
(2) Highly collimated radiation
(3) Highly polarized radiation
(4) Pulsed radiation (Pulse width: about 100 psec)
(5) Radiation with high intensity and high stability

2.1.1. Bending magnet

The purpose of the bending magnet is to change the direction of electron beam. Also it is used for the following two purposes in the electron storage ring [28].

    (1) Production of synchrotron radiation

    (2) Guidance of the electron beam to their reference path in the storage ring

A schematic diagram of the bending magnet is shown in Fig. 2.2.
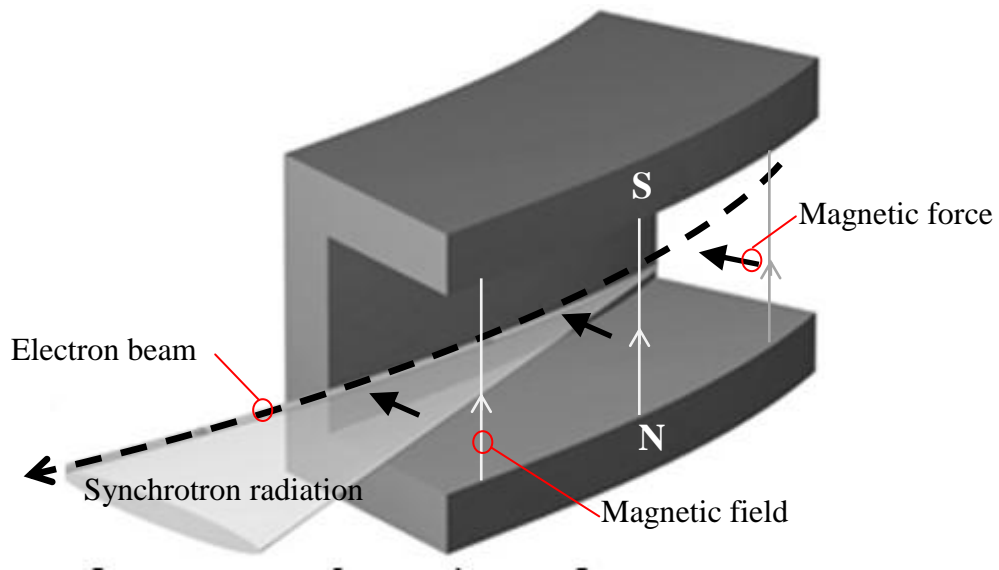
Fig. 2.2: Schematic diagram of the bending magnet.

South and north magnetic poles are indicated as S and N characters, respectively. Magnetic field is produced between those magnetic poles and described by directing arrows with thin lines. The trajectory of electron beam moving through the magnetic field is illustrated by a directing arrow with broken line. The magnetic field influences the direction of the electron beam by a force with a direction (directing arrows with thick line) defined by the right hand rule. As a result, the synchrotron radiation is produced (translucent triangle) and the electrons are guided to their reference path.

2.1.2. Quadrupole magnet

The quadrupole magnet is used to focus the electron beam. It consists of four magnets configured to produce a quadrupole. When electron beam goes through the quadrupole magnets, it is focused into the center of the poles using magnetic field generated from two opposing magnetic north poles and two opposing magnetic south poles. Fig. 2.3 shows the schematic diagram of the quadrupole magnet.
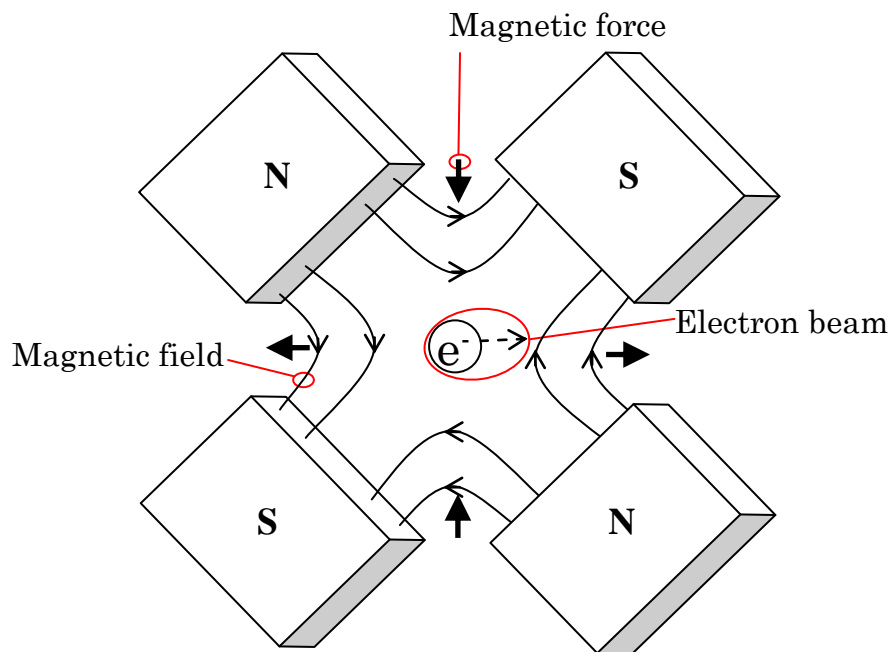
Fig. 2.3: Schematic diagram of the quadrupole magnet.

The boxes with S and N characters show the magnetic poles of south and north, respectively. The directing arrows with thin line and broken line show the magnetic field and trajectory of electron beam, respectively. Also the directing arrows with thick line indicates the direction of the magnetic force to the electron beam.

2.1.3. Injection device

The purpose of the injection device is to introduce the electron beam from the linear accelerator to the reference path in the electron storage ring. It consists of two kinds of magnets called septum and kicker magnets. A schematic diagram of the injection device is shown in Fig. 2.4.

Electron beam for injection

Septum magnet

Kicker magnet

Reference path of electron beam

in storage ring
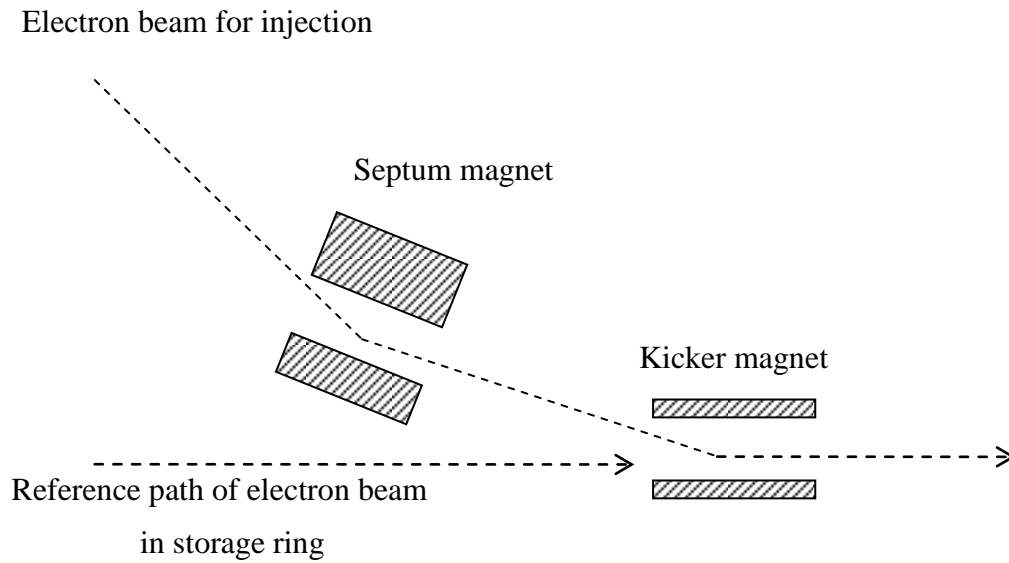
Fig. 2.4: Schematic diagram of the injection device.

In this figure, septum and kicker magnets are drawn with rectangles. The directing arrows with broken line show electron beam for injection and reference path of electron beam. The septum magnet directs the beam toward the closed orbit at the center of the kicker magnet. Then, the kicker magnet performs a correction of remaining angle for the reference path in the electron storage ring.

2.1.4. Insertion device

The insertion device has two major roles: to monochromatize the beam and to make the beam intensity higher. As shown in Fig. 2.5, the device consists of many alternating north and south magnetic poles [29].
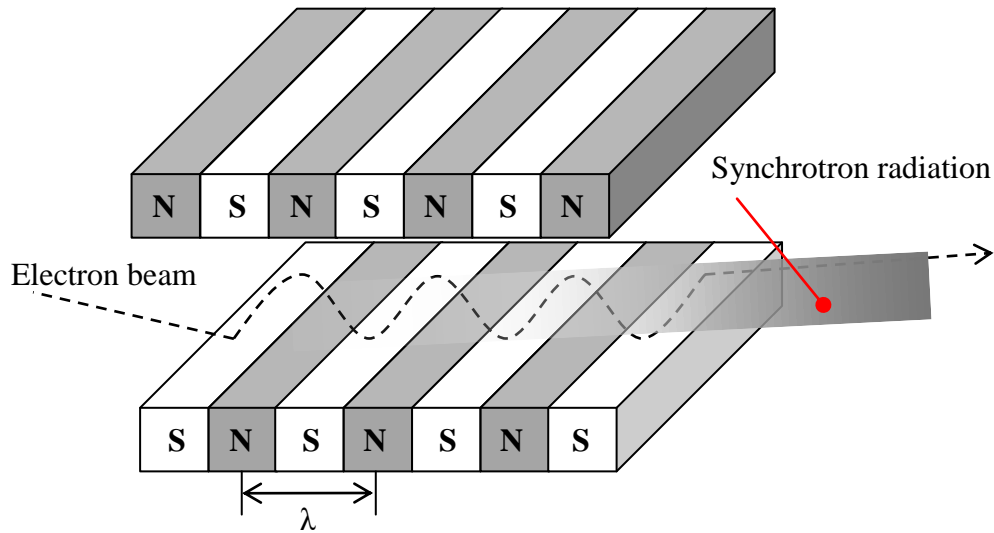
Fig. 2.5: Schematic diagram of the insertion device.

S and N characters in the figure denote the south and north poles, respectively. A directing arrow with broken line indicates electron beam passing through magnetic field between those magnets. Synchrotron radiation is shown as a translucent plate. This device produces an alternating series of inward and outward electron accelerations when the electrons pass through its magnetic field and synchrotron radiations are emitted from the each pole.

Two types of insertion devices are used in the electron storage ring called undulator and wiggler. For the undulator, the magnetic field is relatively weak and monochromatic X-rays with high intensity are possible. The monochromatic photons produced by magnetic field of the undulator overlap and interfere with each other, hence the intensity of the X-rays becomes higher. In the case of strong magnetic field, continuous spectrum with high intensity is possible. This type of insertion device is called "wiggler".

2.1.5. Radio Frequency cavity

The RF cavity is used for accelerating the electron beam. It is a metallic chamber that consists of series of electric poles. A schematic diagram of the RF cavity is shown in Fig. 2.6.
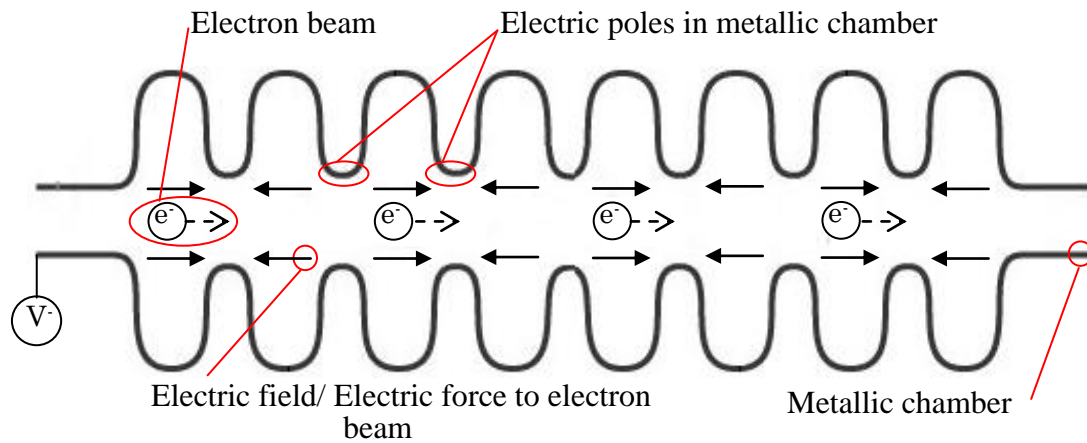
Fig. 2.6: Schematic diagram of the radio frequency cavity.

Directing arrows with thin lines or broken lines indicate electric field or electron beam, respectively. The electric poles are arranged side by side in the RF cavity. A power generator supplies the electric potential to the electric poles, and the positive or negative potentials are always switched on the poles during acceleration of the electron beam. The switching regime is equal with that of the electron motion. Therefore, the electron beam is always influenced by electric force with a direction to which the electron beam flies.

2.2. SOFT X-RAY

Spectrum of the electromagnetic wave is generally classified into seven regions in the order of increasing energy (in the order of decreasing frequency and increasing wavelength): radio waves, microwaves, infrared, visible light, ultraviolet, X-rays and gamma rays. One of the main differences among them is their source. X-rays are generated by the acceleration of electrons, while the gamma rays are generated by nuclear decay. X-rays are also divided into two regions i.e. soft X-rays and hard X-rays. Soft X-rays have energies of about 100 eV to 4000 eV (Wavelength: 0.1 nm ~ 10 nm). The hard X-rays have energy of about 4000 eV or higher (Wavelength: 0.1 nm or shorter) [30].

In this study, we used the "water window", a characteristic region of soft X-rays. The energy region of the water window is between 280 eV and 550 eV. In this region, soft X-rays are mainly absorbed by bio-materials while little by water. Therefore, imaging of hydrated bio-specimens is possible by using soft X-rays in the energy region of the water window. The absorption spectra of water and protein for the energy region of the water window are shown in Fig. 2.7.
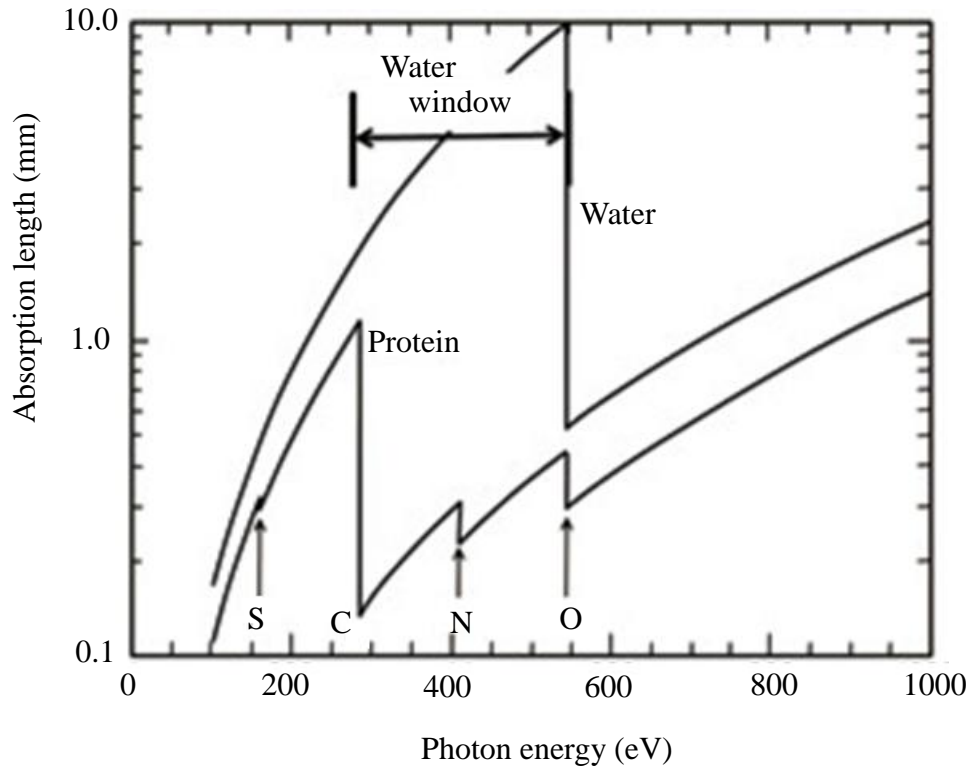
Fig. 2.7: Soft X-ray absorption spectrum for protein and water.

The horizontal axis corresponds to photon energy, whereas vertical axis indicates absorption length that is the distance within which the X-ray beam is absorbed into material. The absorption length is defined as the distance into material where the X-ray intensity decreased to 1/e (e: exponential number) of its incident intensity from the Beer-Lambert law, and it is described in equation (2.2) [31].

$$I(x) = I(0) exp\left\{-\frac{x}{\Lambda}\right\} \quad (2.2)$$

$I(0)$	: Intensity of the incident X-ray
$I(x)$	: Intensity of the transmitted X-ray
x	: Depth of material
Λ	: Absorption length

A model of the Beer-Lambert law describing the transmission process of X-rays into material is shown in Fig. 2.8.
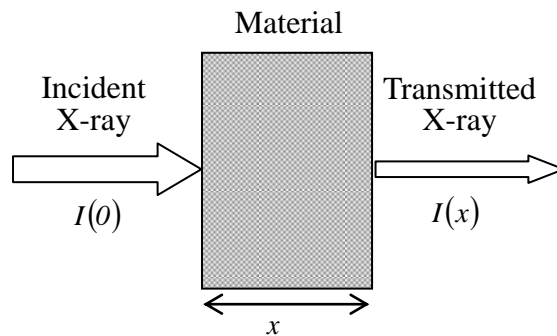
Fig. 2.8: X-ray transmission into material.

In this figure, material is described by a gray rectangle, and X-rays incident to or transmitted through the material are shown by directing arrows.

2.3. FRESNEL DIFFRACTION

Diffraction is a phenomenon where wave turns around an opaque object placed in front of wave propagation. It can be explained qualitatively by Huygens' principle [32].

According to the Huygens' principle, every point of a wave front becomes the source of secondary waves that propagate in all directions with a speed equal to the speed of the original wave.

The diffraction is exhibited if the object size is comparable with the wavelength which are described as a record of interference of the waves. Figure 2.9 shows a schematic diagram of the wave propagation around an opaque object to describe the Huygens' principle.
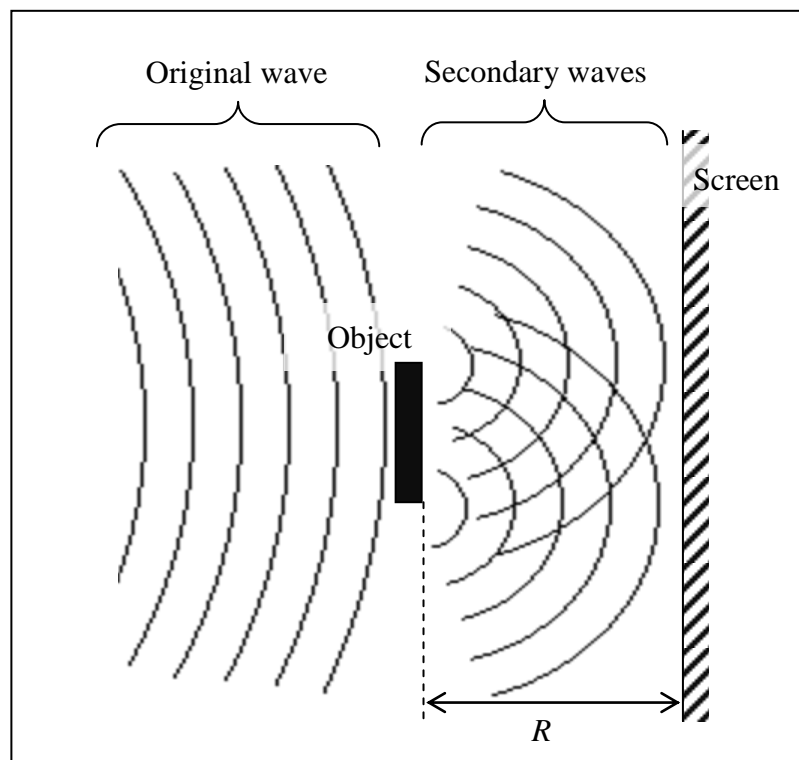
Fig. 2.9: Schematic diagram of wave diffraction process and recording.

The secondary waves from the edges of the object interfere with each other when they overlap, and the wave intensity becomes higher or lower depending on the overlap or deviation of the wave phases, respectively. Figure 2.10 shows an image of intensity distribution recorded on the screen.
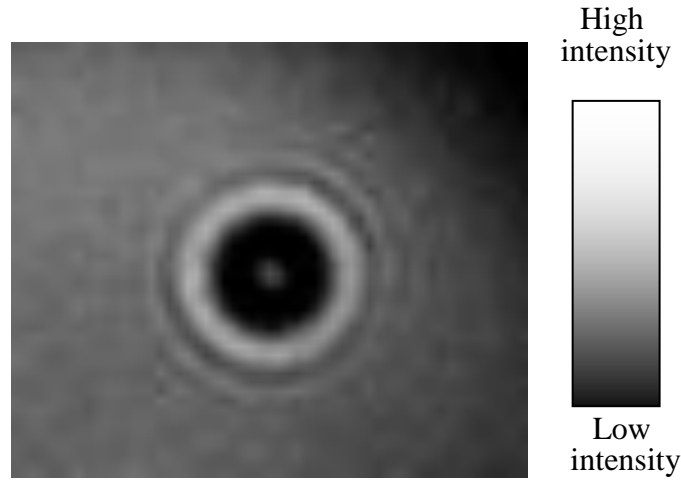
Fig. 2.10: Example image of diffraction fringes recorded on a screen.
(Wave: soft X-rays, Object: Latex particle)

The object was a latex particle with 2 μm diameter and a monochromatic soft X-ray with 700 eV energy was used as the wave source. In this figure, light and dark fringes around the object image and a light point in the center of it due to X-ray diffraction are clearly seen.

A theoretical calculation of the intensity distribution on the screen is also possible from the wave distributions (distribution of complex amplitude) on the object surface. The intensity is defined as square of the wave amplitude and the amplitude distribution on the screen is calculated as an integral of the wave distributions on the object surface (Equation (2.3)) [33].

$$F(x,y) = \frac{A}{i\lambda R} \int_{-\infty}^{\infty}\int_{-\infty}^{\infty} f(x_0, y_0) exp\left\{ik\sqrt{(x-x_0)^2 + (y-y_0)^2 + R^2}\right\} dx_0 dy_0 \quad (2.3)$$

$F(x,y)$: Distribution of complex amplitude on screen

(Intensity distribution: $I(x,y) = |F(x,y)|^2$)

$f(x_0, y_0)$: Distribution of complex amplitude on object surface

x, y : Coordinates on screen

x_0, y_0 : Coordinates on object surface

A : Amplitude of original wave

16

R	: Distance between object surface and screen
I	: Imaginary unit of complex number
λ	: Wavelength
k	: Wave number $(= 2\pi/\lambda)$

Fresnel diffraction is a diffraction behavior that is possible to calculate by a method proposed by Augustin Jean Fresnel. The method calculates diffraction pattern on the screen from the distribution of waves passing through an aperture or turning around an object in the case that the object (or aperture) is placed close to the screen. In other words, it indicates a case of diffraction described in Fig. 2.9 where the object size is sufficiently smaller than the distance between the object surface and the screen. The condition formula is as follows:

$$R^3 >> \frac{1}{8\lambda}\left((x-x_0)^2 + (y-y_0)^2\right)$$

The Fresnel equation (equation (2.4)) is defined from the above condition and the equation (2.3).

$$F(x,y) = \frac{A}{i\lambda R} exp\{ikR\}\int_{-\infty}^{\infty}\int_{-\infty}^{\infty} f(x_0, y_0)exp\left\{\frac{ik}{2R}\left((x-x_0)^2 + (y-y_0)^2\right)^2\right\}dx_0 dy_0 \quad (2.4)$$

2.4. FRESNEL ZONE-PLATE

In this study, a zone plate was used to make a point source of X-rays from synchrotron radiation. This section introduces the principles and theories for a zone-plate.

The purpose of a zone plate is to focus X-ray beam at a point. It is constructed with radially symmetric rings where opaque and transparent zones are arranged with a mutually turn. The incident X-rays diffract around the opaque zones and focused at its focal points by the interference of the diffracted X-rays. A schematic diagram of a Fresnel Zone plate is shown in Fig. 2.11.
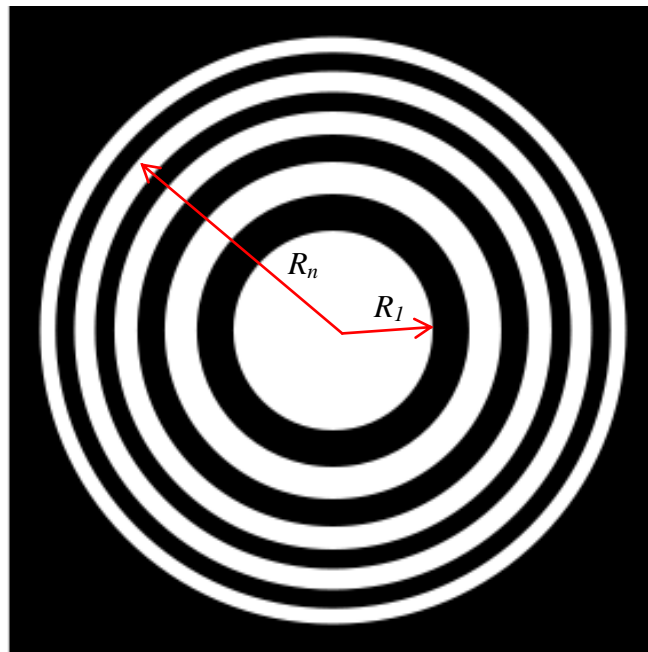
Fig. 2.11: Fresnel zone-plate.

The opaque zones of the Fresnel zone plate are shown with black rings in the figure and the zones are numbered from the smallest one to bigger sizes of the zones. The zone radius with number n is calculated by equation (2.5) [33].

$$R_n = \sqrt{n\lambda f} \quad (2.5)$$

n : Positive integers for the zone numbers

λ : Wavelength of incident X-rays

f : Focal distance (Distance between central point of zone-plate

and focal point)

It is possible to show the focal distance from equation (2.5) as follows (equation (2.6)).

$$f = \frac{R_n^2}{n\lambda} = \frac{R_1^2}{\lambda} \quad (2.6)$$

Several focal positions are shown in Fig. 2.12 where a parallel beam of X-rays is irradiated to the zone-plate along its axis.
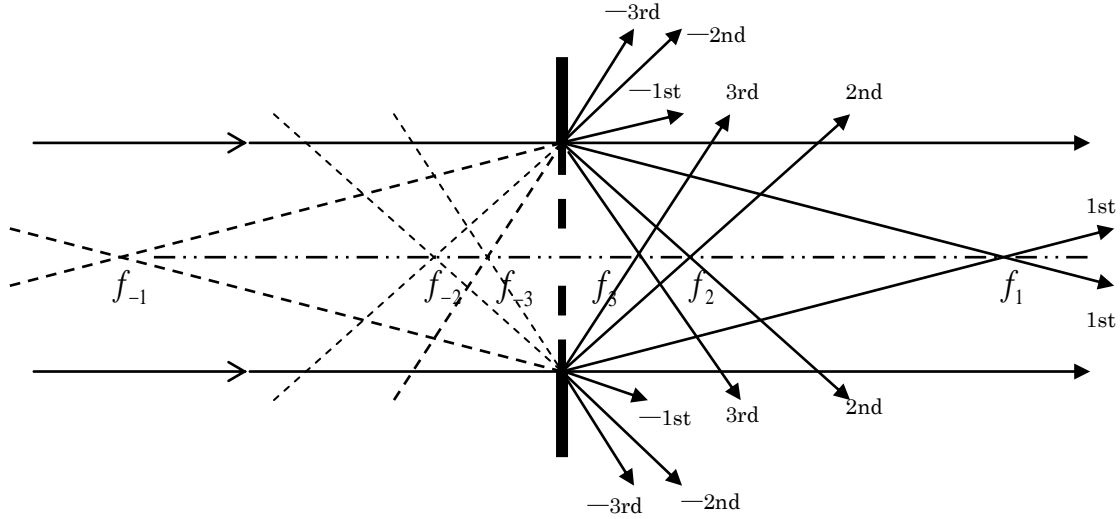
Fig. 2.12: Focal positions of parallel X-rays on Fresnel zone-plate.

In this figure, X-rays are shown with thin lines. Continuations of diverged X-rays in the opposite direction of its propagation are shown with broken lines. The focal points of the X-rays are defined as follows (Equation (2.7)) [34]:

$$0^{th} \quad f_0 = \infty$$

$$+1^{st} \quad f_1 = \frac{r_1^2}{\lambda} \qquad -1^{st} \quad f_{-1} = -f_1$$

$$+2^{nd} \quad f_2 = \frac{f_1}{3} \qquad -2^{nd} \quad f_{-2} = -f_2 \qquad (2.7)$$

$$+3^{rd} \quad f_3 = \frac{f_1}{5} \qquad -3^{rd} \quad f_{-3} = -f_3$$

Positions of the focal points varied depending on the wavelength of X-rays and diffraction orders as shown in Fig. 2.12 and equations (2.6, 2.7). Therefore, a pinhole is usually placed between the zone plate and the focal point in accordance with the condition of the wavelength and requested diffraction order. Thus a spherical wave component with particular characteristics could be isolated.

2.5. FOURIER TRANSFORMATION AND INVERSE FOURIER TRANSFORMATION

In this section, theoretical basis for calculations of the Fresnel diffraction and inverse Fresnel diffraction is introduced.

First, we denote the Fresnel equation (2.4) in one dimension. Then, by briefing the part of constant number before the integral sign of the equation for Fresnel diffraction and multiplying it with $\sqrt{\lambda R}$, it becomes the same form as the Fourier transformation (FT). Therefore it gives the possibility to calculate the wave distributions on the screen and the object surface by using the equations of Fourier and inverse Fourier transformations (IFT). The FT and IFT equations are shown in equation (2.8) and (2.9), respectively [35].

$$\text{FT:} \quad F(x) = \frac{1}{\sqrt{\lambda R}} \int_{-\infty}^{\infty} f(x_0) \, exp\left\{ \frac{ik}{2R}(x - x_0)^2 \right\} dx_0 \quad (2.8)$$

$$\text{IFT:} \quad f(x_0) = \frac{1}{\sqrt{\lambda R}} \int_{-\infty}^{\infty} F(x) \, exp\left\{ -\frac{ik}{2R}(x - x_0)^2 \right\} dx_0 \quad (2.9)$$

$F(x)$	: Distribution of complex amplitude on screen
$f(x_0)$	: Distribution of complex amplitude on object surface
x	: Coordinate on screen
x_0	: Coordinate on object surface
R	: Distance between object surface and screen
i	: Imaginary unit of complex number
λ	: Wavelength
k	: Wave number($= 2\pi/\lambda$)

An image describing the coordinates on the object surface and the screen for diffraction calculation is shown in Fig. 2.13.
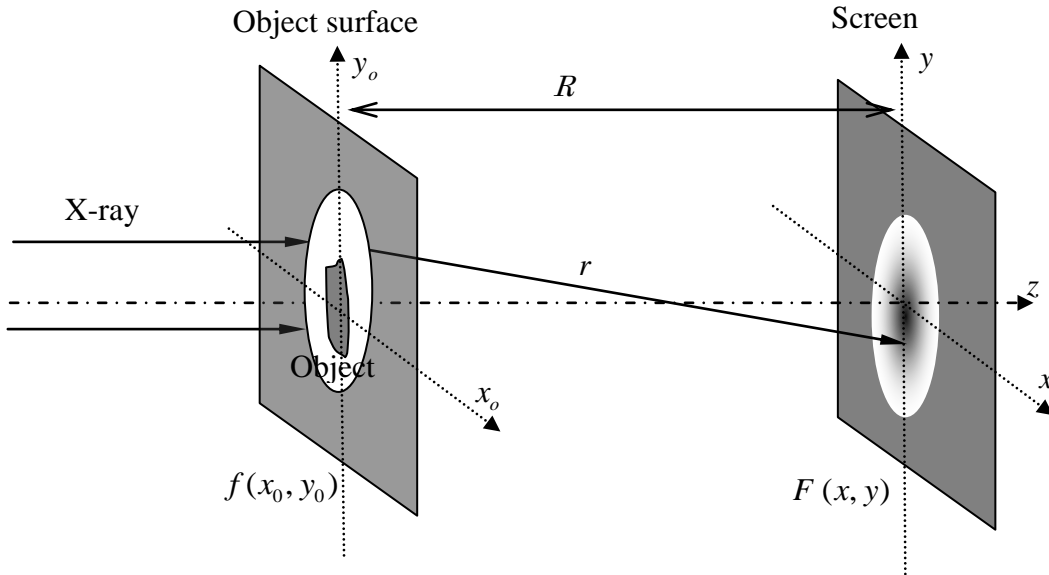
Fig. 2.13: Coordinates for diffraction calculation.

In order to calculate the equations of FT and IFT by computer, their discrete forms are necessary. Therefore the discrete equations of FT and IFT are defined by approximating the integrals of equations (2.8) and (2.9). The discrete equations are shown in equations (2.10) and (2.11).

$$\text{FT:} \quad F(mT) = \frac{T_0}{\sqrt{\lambda R}} \sum_{n=0}^{N-1} f(nT_0) exp\left\{ \frac{i\pi}{\lambda R}(mT - nT_0)^2 \right\} \quad (2.10)$$

$$\text{IFT:} \quad f(nT_0) = \frac{\sqrt{\lambda R}}{T_0 N} \sum_{n=0}^{N-1} F(mT) exp\left\{ -\frac{i\pi}{\lambda R}(mT - nT_0)^2 \right\} \quad (2.11)$$

N	: Total number of sampling
T_0	: Sampling interval on object surface
T	: Sampling interval on screen
n, m	: Positive integers $(= 0, 1, \dots, N-1)$

For a reversible relation between these equations (2.10) and (2.11), a restraint condition for the sampling number and intervals (RC-1) is necessary as shown in equation (2.12).

$$T_0 T = \frac{\lambda R}{N} \quad (2.12)$$

To calculate the discrete FT equation for sampling of N times, calculations of N^2 times which require an enormous amount of time are needed. In order to reduce the calculation time, a fast Fourier Transformation (FFT) method is used. To define the FFT method, first we change the discrete FT equation (2.10) to the equation (2.13) and (2.14).

$$F(mT) = \frac{T_0}{\sqrt{\lambda R}} \sum_{n=0}^{N-1} f(nT_0) exp\left\{ i\pi \frac{(mT)^2 - 2mnTT_0 + (nT_0)^2}{\lambda R} \right\} \quad (2.13)$$

$$F(mT) = \frac{T_0}{\sqrt{\lambda R}} exp\left\{ i\pi \frac{(mT)^2}{\lambda R} \right\} \sum_{n=0}^{N-1} f(nT_0) exp\left\{ i\pi \frac{(nT_0)^2}{\lambda R} \right\} exp\left\{ -i2\pi \frac{mnTT_0}{\lambda R} \right\} \quad (2.14)$$

By using the restraint condition of equation (2.12) and an additional replacement of $f'(nT_0) = f(nT_0) exp\left\{ i\pi \frac{(nT_0)^2}{\lambda R} \right\}$, the following equation (2.15) is formulated.

$$F(mT) = \frac{T_0}{\sqrt{\lambda R}} exp\left\{ i\pi \frac{(mT)^2}{\lambda R} \right\} \underline{\sum_{n=0}^{N-1} f'(nT_0) exp\left\{ -i2\pi \frac{mn}{N} \right\}} \quad (2.15)$$

The underlined part of the equation (2.15) has the same form as that of discrete FT which the FFT is possible, because exponential part has a symmetric property with N period. The property was formulated in equation (2.16) by using a replacement of $W^{mn} = exp\left\{ -i2\pi \frac{mn}{N} \right\}$.

$$W^N = 1 \quad and \quad W^k = W^{k+N} = W^{k+2N} = ... \quad (2.16)$$

k : Positive integer

In order to show the symmetric property, the equation (2.15) is shown in matrix form by using an addition replacement of $F(m) = F(mT)$ and $f'(n) = f'(nT_0)$. Also, the

constant part in front of summation of the equation was omitted. Equation (2.17) [33] shows the matrix.

$$
\begin{bmatrix} F(0) \\ F(1) \\ F(2) \\ \vdots \\ F(N-1) \end{bmatrix} = \begin{bmatrix} W^0 & W^0 & W^0 & \cdots & W^0 \\ W^0 & W^1 & W^2 & \cdots & W^{N-1} \\ W^0 & W^2 & W^4 & \cdots & W^{2(N-1)} \\ \vdots & \vdots & \vdots & \ddots & \vdots \\ W^0 & W^{N-1} & W^{2(N-1)} & \cdots & W^{(N-1)^2} \end{bmatrix} \times \begin{bmatrix} f'(0) \\ f'(1) \\ f'(2) \\ \vdots \\ f'(N-1) \end{bmatrix} \quad (2.17)
$$

As shown in the matrix, calculations (multiplications) of N^2 times are needed for the discrete FT. However, same calculations are repeated for each symmetric part. In the FFT, more simple calculation is possible without the repeated calculations for the symmetric parts. Consequently the number of the calculations becomes $N \times log_2(N)/2$ times by using the FFT. To use the FFT, we need to adjust the number of samples to be $N = 2^k$ (k : positive integer).

CHAPTER 3: INSTRUMENT OF PROJECTION MICROSCOPY

3.1. ELECTRON STORAGE RING OF PHOTON FACTORY, HIGH ENERGY ACCELERATOR RESEARCH ORGANIZATION

In this study, we used the electron storage ring of Photon Factory (PF) of High Energy Accelerator Research Organization (KEK), Tsukuba, Japan as a soft X-ray source. Main parameters of the PF electron storage ring [36] are shown in Table 3.1.

Table 3.1: Main parameters of PF electron storage ring.

-	Parameter
Beam energy	2.5 GeV
Initial beam current	450 mA
Circumference	187 m
Bending radius	8.66 m
Beam emittance	34.6 nm*rad
Beam lifetime	30~35 h (at 450mA)
Average ring pressure	$6*10^{-8}$ Pa (at 400mA)
Radiation loss	400 keV/turn
Number of bunches	280
Number of bending magnets	28
Number of quadrupole magnets	78
Number of insertion devices	8
Number of RF cavities	4
RF frequency	500.1 MHz
Stability of SR beam position	SR beam drift is less than 20 μm during the whole day (at 20 m from source point)

Layout of PF electron storage ring and positions of experimental stations [37, 38] are shown in Fig. 3.1.
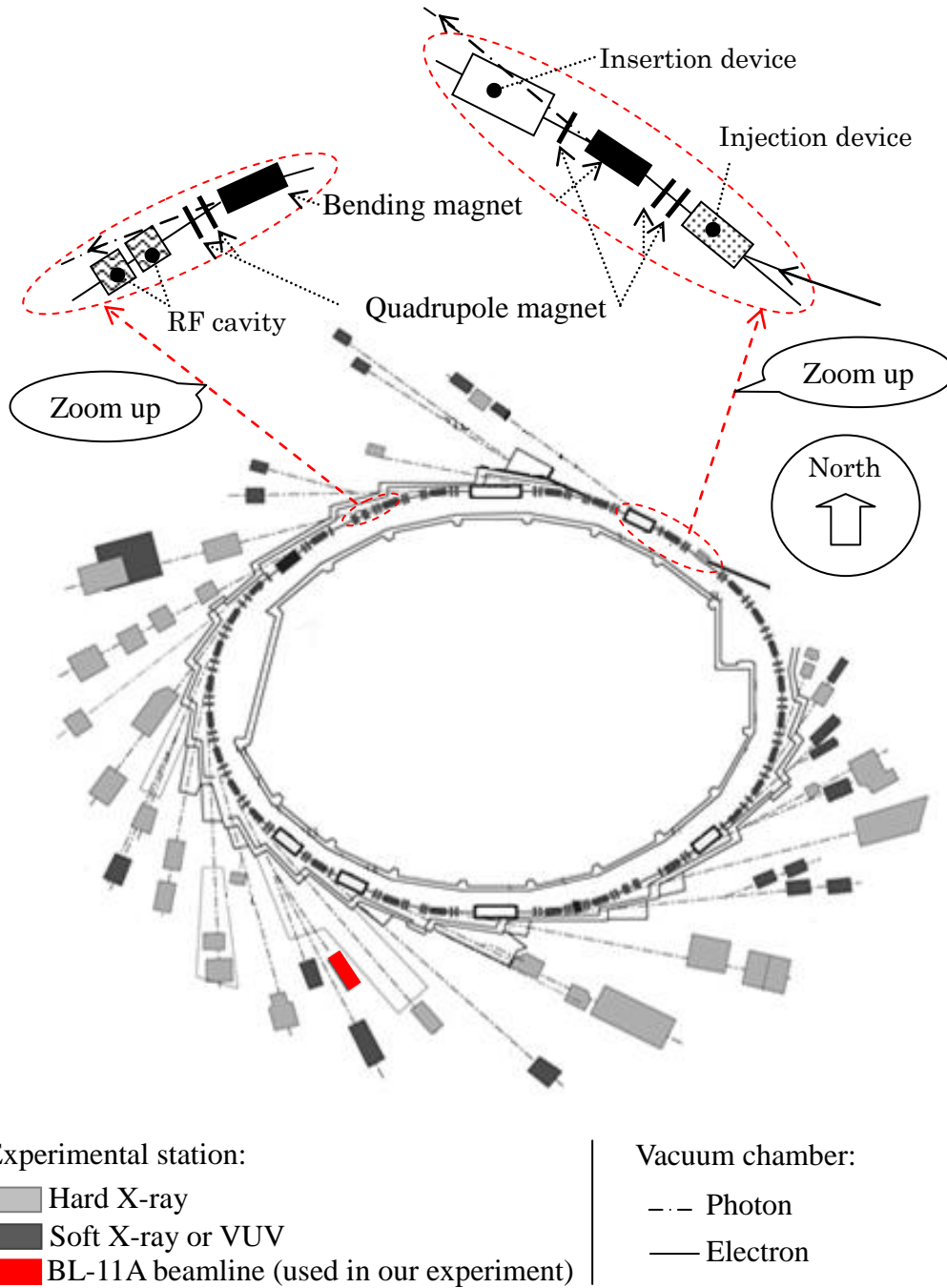
Fig. 3.1: Layout of PF electron storage ring and positions of experimental stations.

Experimental stations are shown with gray and black plates for hard X-rays and soft X-rays or vacuum ultra violet (VUV) radiation, respectively. The experimental station for BL-11A beamline used in our experiment is shown by a red square. Some representative parts of the storage ring in red and broken lines are zoomed up on top of the figure and the devices in the zoomed up parts are explained. The bending and quadrupole magnets are shown with large and small black squares, respectively. The insertion and injection devices and RF cavities are also indicated as white squares and by squares filled with black points and waves, respectively.

In our experiment, a bending magnet with number B11 [39] which produces photon energy spectrum as shown in Fig. 3.2, was used
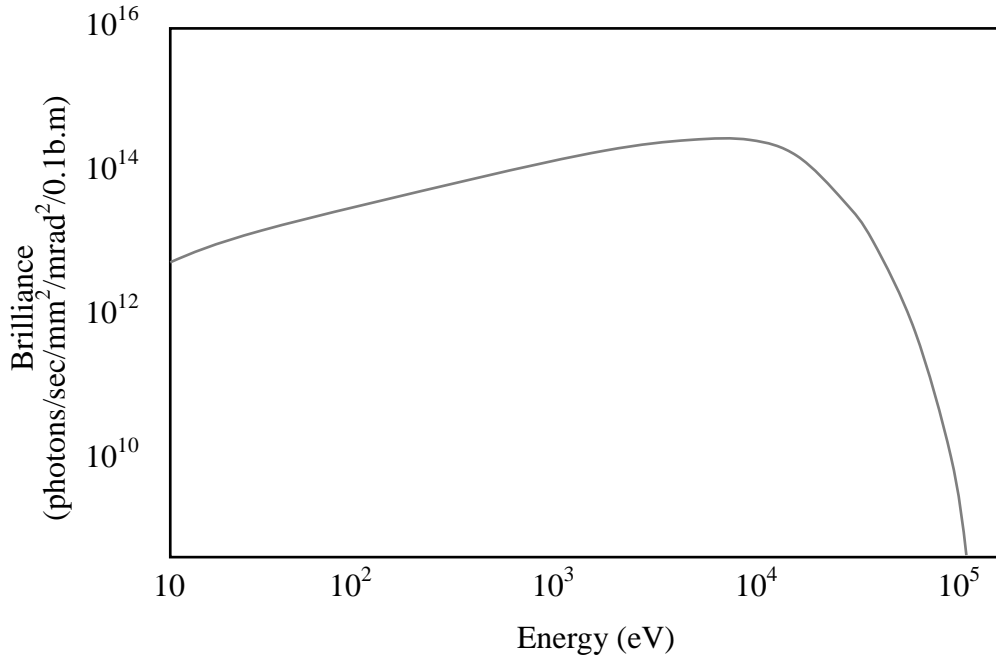
Fig. 3.2: Photon energy spectrum produced by bending magnet in PF electron storage ring, KEK.

Horizontal axis corresponds to photon energy, while vertical axis corresponds to brilliance of the photon beam. The brilliance is defined as the equation (3.1) [40].

$$B = \frac{d^4 N}{dt \cdot d\Omega \cdot dS \cdot (d\lambda \div \lambda)} \quad (3.1)$$

N	: Number of photon	
t	: Time	
Ω	: Solid angle	
S	: Beam size (cross section)	
λ	: Wavelength	

BL-11A beamline provides soft X-rays in the energy range between 70 eV and 1900 eV with a grazing-incidence monochromator from the X-ray spectrum shown in Fig. 3.2. Layout of the BL-11A beamline [39] is shown in Fig. 3.3.
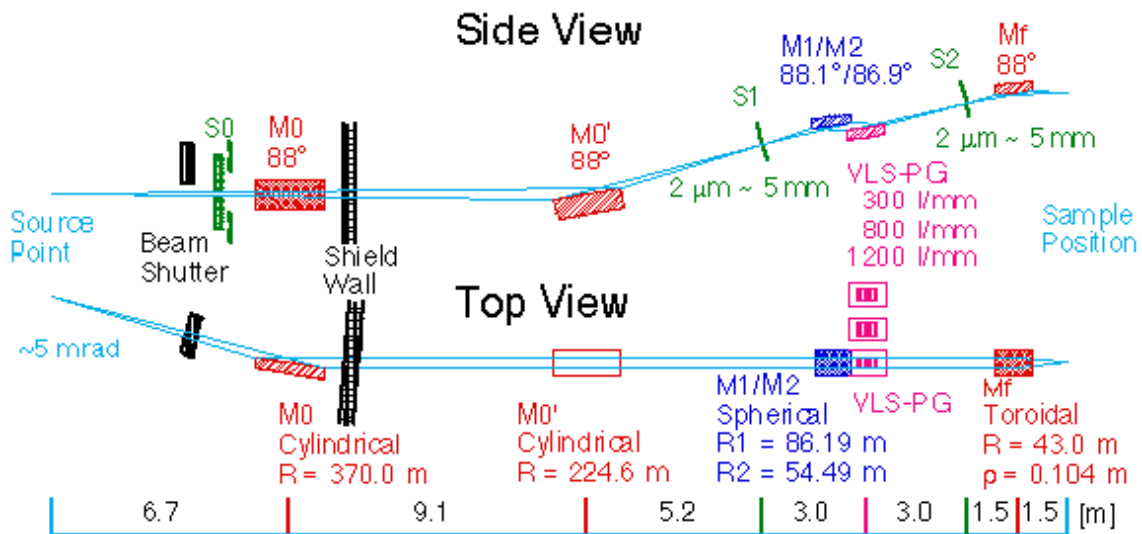
Fig. 3.3: Layout of BL-11A beamline of PF, KEK.
S0~S2: Apertures or slits, M0 and M0': Cylindrical mirrors, M1 and M2: Spherical mirrors, Mf: Toroidal mirror, VLS-PG: Varied-Line-Spacing Plane Grating.

The figure describes the layout of the beamline viewed from the top view and from the side view. In this beamline, the synchrotron radiation from the bending magnet B11 (maximum horizontal acceptance of 5 mrad) is reflected by two cylindrical mirrors M0 and M0', first. The reflected beam is monochromatized and focused by a grazing-incidence monochromator consisting of spherical mirror (M1 or M2), and varied-line-spacing plane grating (VLS-PG), between the entrance and the exit slits (S1 and S2). Finally, it is refocused by a toroidal mirror (Mf) to the sample position. S0 is an aperture to pass center or off-axis beams for linearly or elliptically polarized soft X rays, respectively.

The monochromator is equipped with mechanisms to exchange two spherical mirrors (M1 and M2) with different incident angles and three gratings with different

groove densities of 300 l/mm, 800 l/mm and 1200 l/mm. The mechanism enables us to obtain appropriate energy ranging from 70 eV to 1900 eV without vacuum breakdown. A grating with groove density of 800 l/mm was used in our experiment. Available energy spectrum in the combination of this grating and the mirror M2 illustrated in Fig. 3.3 is shown in Fig. 3.4 [39].
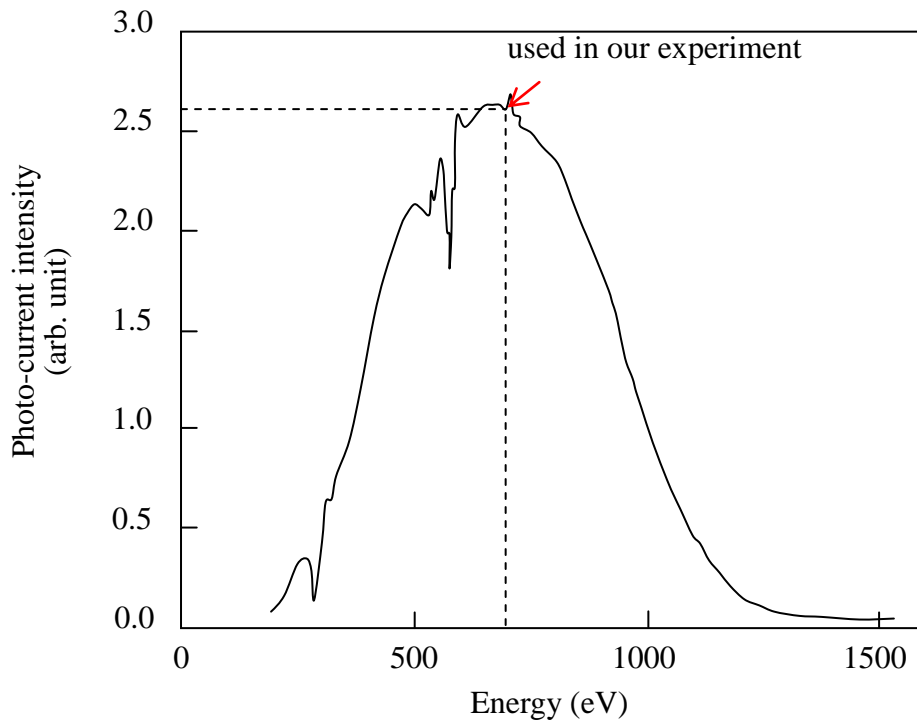
Fig. 3.4: Available energy spectrum of photon for a grating with groove density of 800 l/mm.

The horizontal axis and vertical axis show the available photon energy and photo-current intensity, respectively. The graph shows the distribution of the available X-ray energy. In our experiment, a monochromatic spectrum with an energy of 700 eV was chosen which is indicated by the broken line on the figure. The energy resolution for the spectrum was 1.4 eV.

3.2. PROJECTION MICROSCOPY SYSTEM

We installed a projection microscopy system at the experimental station for BL-11A beamline of PF, KEK (Fig. 3.5). In order to make a point source from soft X-ray beam of the beamline, the projection system was constructed with a zone-plate and a pinhole which is located at the focal point of the zone-plate. A back-illuminated X-ray CCD camera was used for imaging. For the imaging, a specimen was placed between the pinhole and the CCD camera and magnified images of the specimen were captured on the CCD screen as projection images. Optical layout of the projection microscopy system is shown in Fig. 3.5.
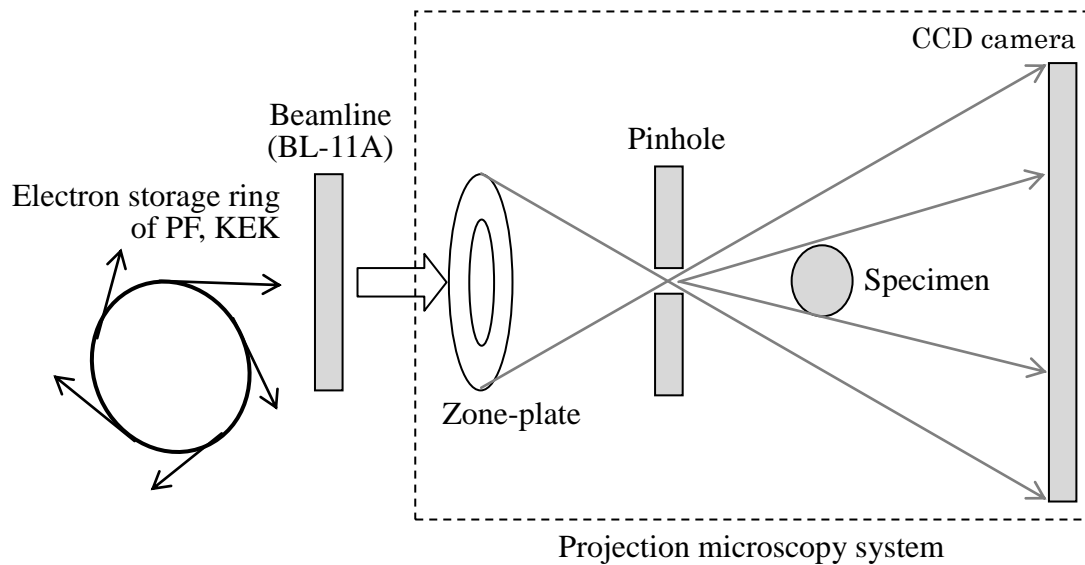
Fig. 3.5: Optical layout and a schematic diagram of structure of the soft X-ray projection microscopy.

The projection microscopy system is shown in a rectangle with broken line. A zone-plate, a pinhole, a specimen and a CCD camera are shown in the rectangle from the left to the right direction, side by side. The electron storage ring and the beamline are shown in the left side of the rectangle. Zooming is easily performed by moving the specimen along axis of the projection system. For zooming up, the specimen closes to the pinhole. In contrast, it moves off from the pinhole for zooming out.

A photo image of the projection system which shows just an exterior image is presented in Fig. 3.6. The zone-plate and the pinhole are contained in the high vacuum chamber. The specimen is placed in the chamber with lower vacuum just behind a

window of the vacuum bulkhead. Behind the vacuum chamber, a CCD camera system is connected. The position of the specimen is also indicated.
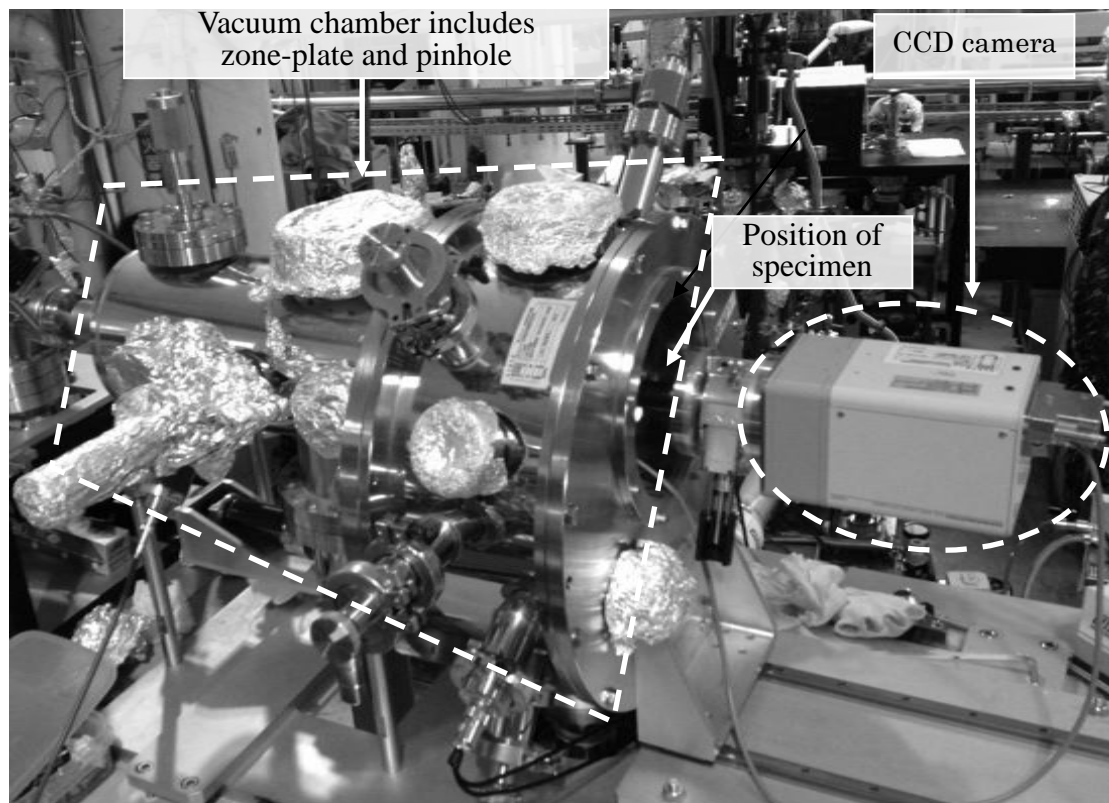
Fig. 3.6: Soft X-ray projection system installed for experiment.

The details of the zone-plate, pinhole and CCD camera system are introduced in the next subsections (3.2.1 ~ 3.2.3).

3.2.1. Zone-plate

In this study, we used a Fresnel zone-plate (FZP) with binary type made by NTT Advanced Technology Corporation. The structure of FZP is schematically shown in Fig. 3.7.

(a) x-y cross section
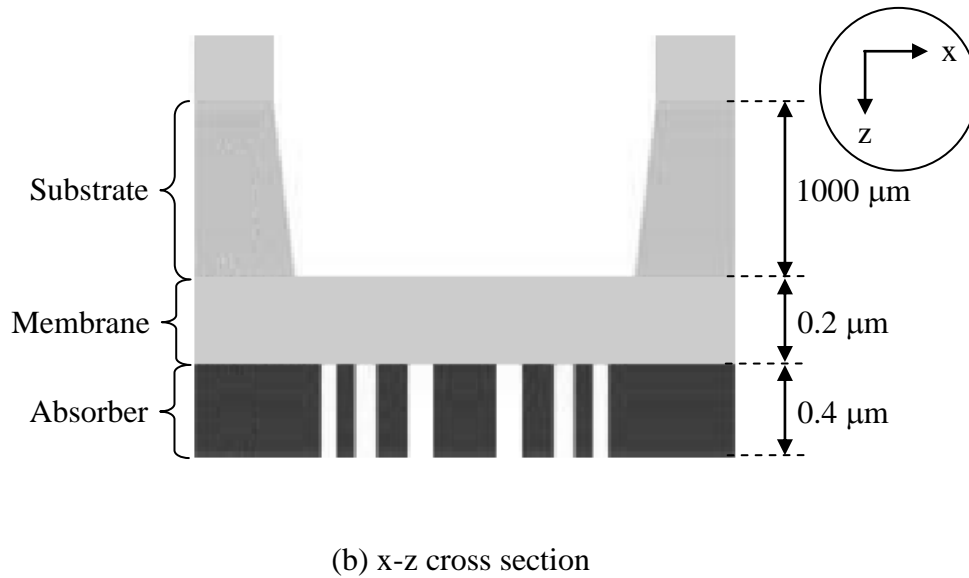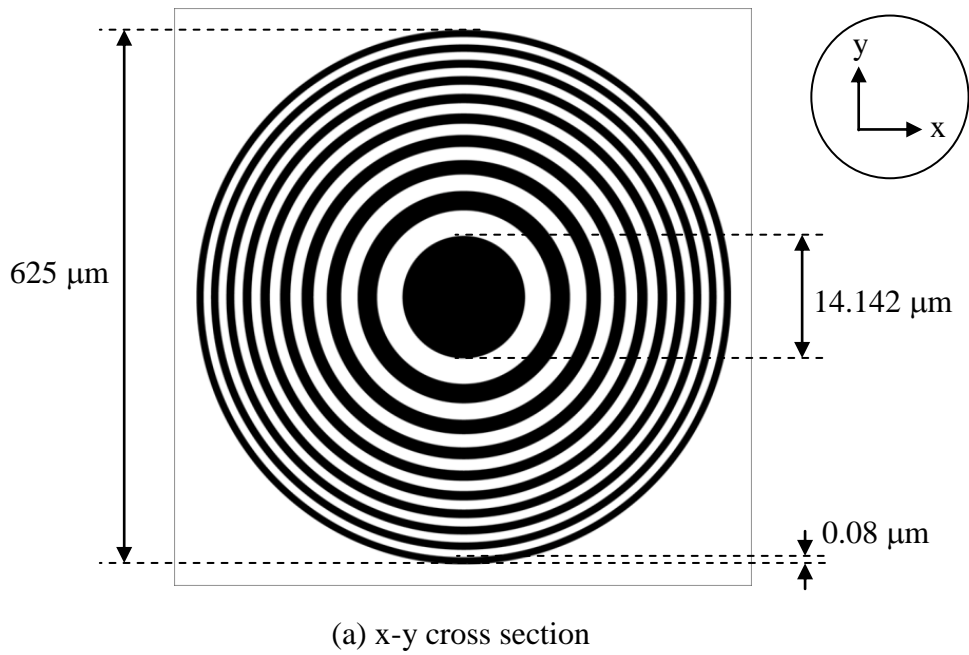
(b) x-z cross section

Fig. 3.7: Structure of Fresnel zone-plate.

Fig. 3.7 (a) and (b) show x-y and x-z cross-sectional views, respectively. The FZP consists of three layers that are called absorber, membrane and substrate. A membrane with thickness of 0.2 µm is in between an absorber with thickness of 0.4 µm and a substrate with thickness of 1 mm. The absorber has a structure of radially symmetric rings, known as Fresnel zones. The main parameters of this zone-plate are summarized in Table 3.2.

Table 3.2: Main parameters of a Fresnel zone-plate used in this study.

Items		Parameters
Substrate	Material	Si
	Thickness	1000 µm
	Shape	10 mm square
Membrane	Material	SiN
	Thickness	0.2 µm
Absorber	Material	Ta
	Thickness	0.4 µm
	Total number of zone	1952
	Maximum diameter	625 µm
	Radius of inner most circuit	7.071 µm
	Minimum zone width (outer most zone)	0.08 µm

3.2.2. Pinhole

The pinhole supplied by Kanagawa Academy of Science and Technology (KAST) was made using a Focused Ion Beam (FIB) technique [41] which is applied particularly in nanofabrication process. In the FIB technique, ion beam from a liquid metal ion source was focused by electric and magnetic fields, and the material for the pinhole was placed at the focal point of the ion beam to create a hole.

A model of the pinhole is shown in Fig. 3.8.

(a) x-y cross section
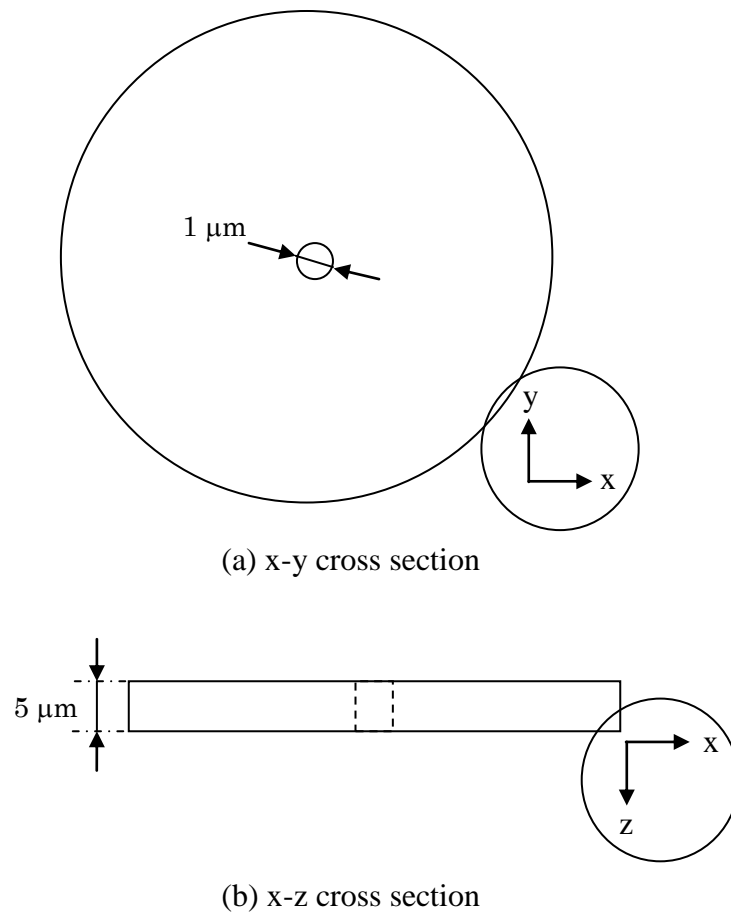
(b) x-z cross section

Fig. 3.8: Pinhole.

Fig. 3.8 (a) and (b) show x-y and x-z cross-sectional views, respectively. The pinhole was made from platinum material with 5 μm depth and 1 μm diameter.

3.2.3. CCD camera

In this study, a back-illuminated X-ray CCD camera (Hamamatsu Photonics C4880-30-26WS) was used. The configuration of the CCD camera system is shown in Fig. 3.9.
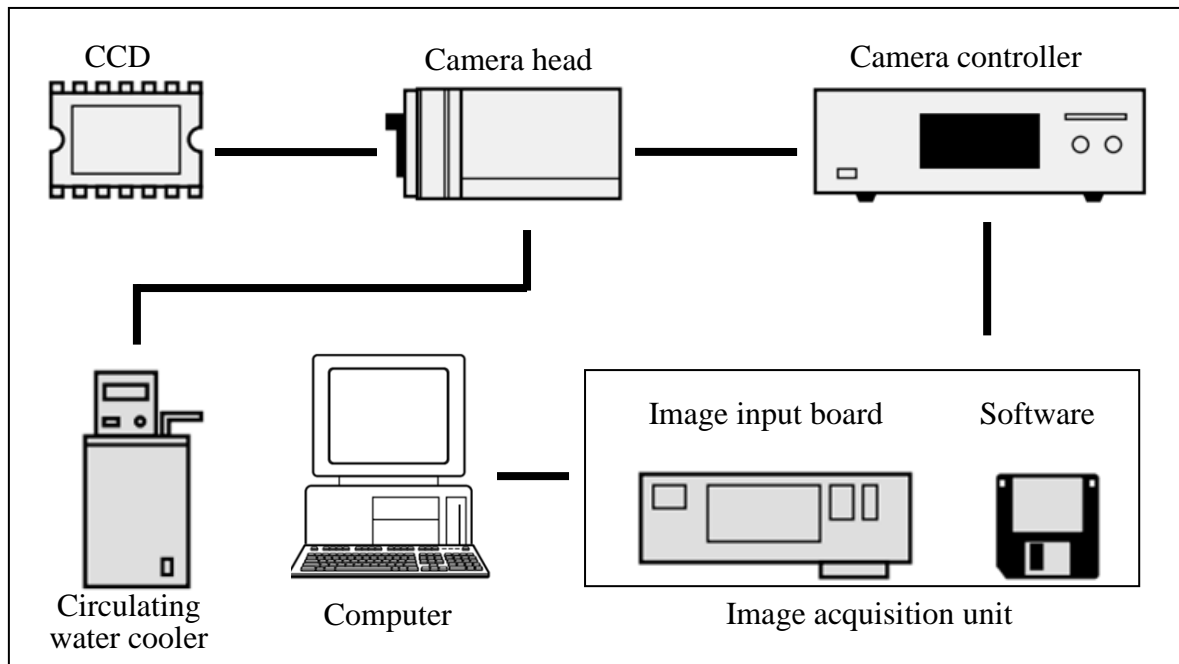
Fig. 3.9: Configuration of CCD camera system.

It consists of a back-thinned illuminated CCD, a hermetically vacuum-sealed head, a circulating water cooler for the camera head, camera controller, image acquisition unit and computer. To import images captured with the CCD camera, from the image acquisition unit to the computer, a software "Image-Pro Plus" (Media Cybernetics, USA) was used. The image properties are as follows:

- Pixel-pitch: 24.8 μm
- Image size: 512*512 pixels
- Bit depth: 16 bit

Fig. 3.10 shows the photo images of the CCD camera system including a set of the camera head and the CCD (1) and the circulating water cooler (2).
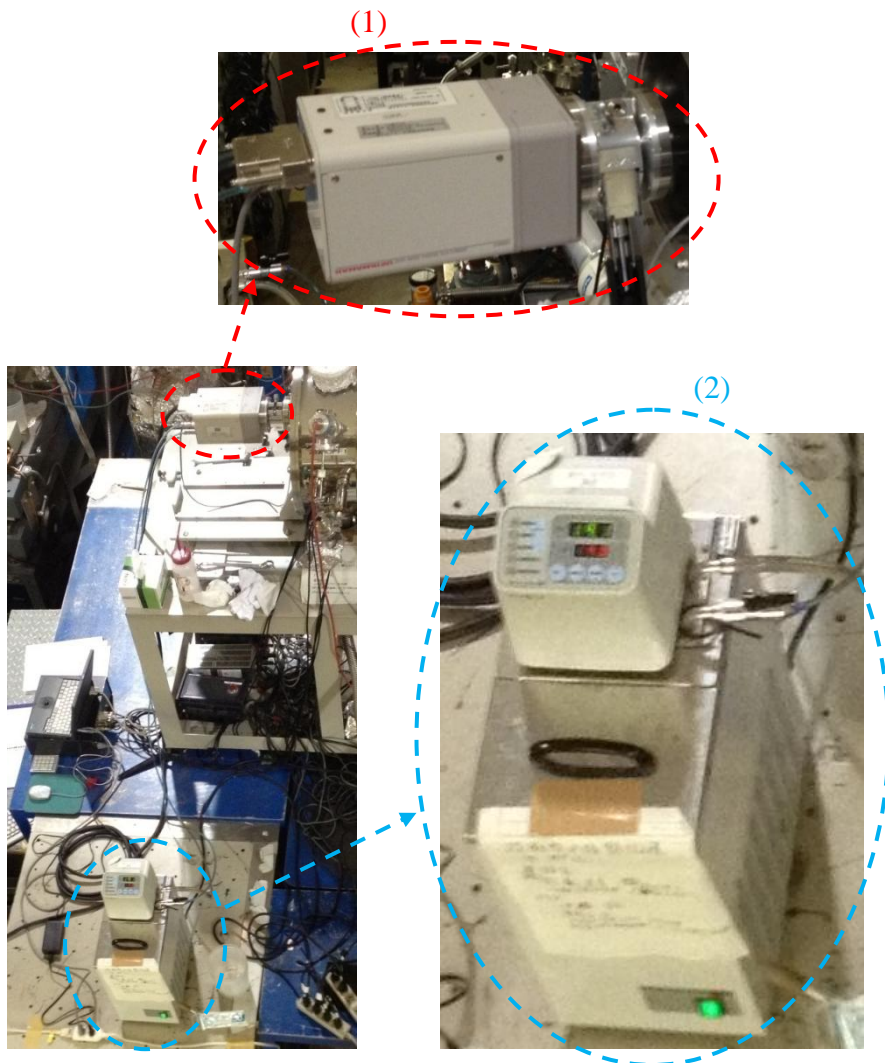
(1) Set of CCD and camera head, (2) Circulating water cooler

Fig. 3.10: CCD camera system installed for experiment.

CHAPTER 4: MATERIALS AND METHODS

4.1. PROJECTION METHOD AND CONDITION

Projection imaging was performed at various magnifications. The magnification was adjusted by moving the specimen between the pinhole and the CCD screen. As illustrated in the optical layout (Fig. 4.1), it can be calculated as a ratio of the distance from pinhole to CCD screen and to specimen location (equation (4.1)).

$$X = \frac{D}{d} \quad (4.1)$$

X : Magnification

D : Distance between pinhole and CCD screen

d : Distance between pinhole and specimen
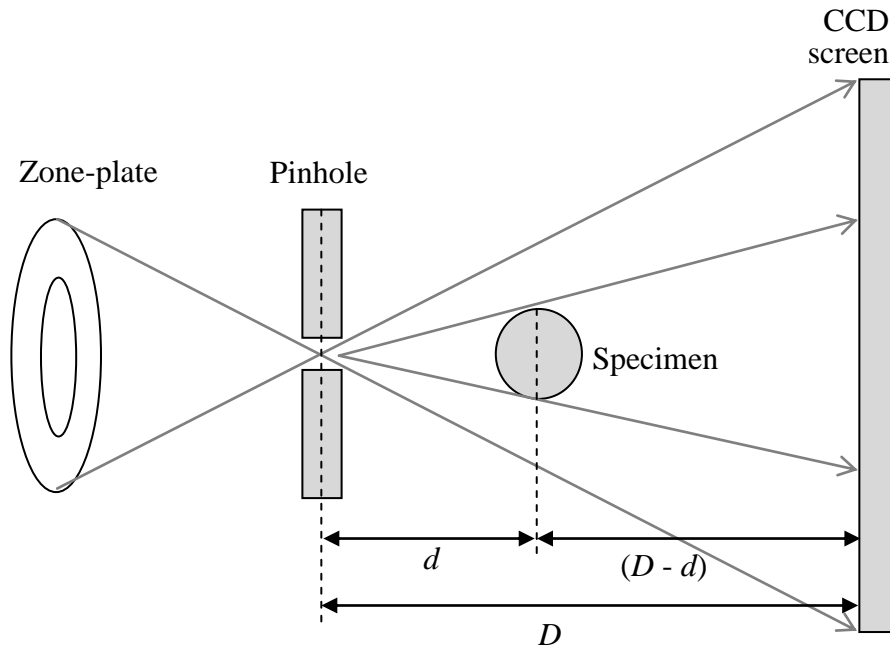
Fig. 4.1: Optical layout of projection system of the soft X-ray projection microscopy.

In the figure, soft X-rays are shown in gray lines. Soft X-rays, which are focused on

the center of the pinhole by the zone-plate, propagate to the CCD screen. Some of the X-rays penetrate through the specimen. The X-rays unshielded or penetrated through the specimen are then recorded on the CCD screen. As shown in equation (4.1), when the specimen is placed close to the pinhole, imaging with high magnification is possible. Typical experimental conditions are summarized in Table 4.1.

Table 4.1: Typical experimental conditions.

-	Values
X-ray energy	700 eV
Focal distance of zone-plate	28.25 mm
Focal spot size of zone-plate	97.6 nm
Pinhole diameter	0.5 or 1 μm
Distance between pinhole and CCD screen	329 mm
Distance between pinhole and specimen	0.5~7 mm
Coherence length at the specimen position (for the pinhole with 0.5 μm diameter)	1.77~24.8 μm
Temporal coherence (Energy resolution)	0.89 μm (1.4 eV)
Magnification	47~658 times
Projection time	3 min

4.2. SPECIMEN PREPARATION

4.2.1. Chromosome

Chromosome preparation was made from cultured human lymphocyte cell line (IM-9) on a silicon nitride window with 1 mm square in size and 100 nm in thickness supported by a center-hollowed silicon substrate with 5 mm square in size and 380 µm in thickness according basically to the standard protocol for light microscopic observation with some minor modifications [41]. A brief flow of the chromosome preparation is as follows.

(1) The cells in early logarithmic growth phase ($2\sim3*10^5$ cells /ml) are arrested in mitotic phase by treating with 50 µg/ml of colcemid at 37 °C for 5 hours and centrifuged at 1000 rpm for 5 min.

(2) The precipitated cells were resuspended in a hypotonic solution (75 mM of KCl or 0.6 % of sodium citrate) at 37 °C, and kept for 20 min at the same temperature for swelling and then fixed with Carnoy fixative (a mixture of methanol/glacial acetic acid 3:1).

(3) A small volume (ca. 30 - 40 µl) of the fixed cell suspension was dropped onto the silicon nitride window and air dried.

In some cases, the window with chromosome specimen was washed with fresh fixative to remove cytoplasmic debris around the chromosomes before the specimen was dried up completely. The background of the window surface became rather clean with little loss of chromosomes by this wash.

An example image of the chromosomes prepared for the projection experiment is shown in Fig. 4.2. The image was captured using an optical microscopy. As shown in the image, the chromosomes with their characteristic morphology could be successfully be prepared. Especially, the chromosomes in the red circle have relatively good shape without overlapping of excess bending compared to others. Therefore, we chose those chromosomes for our projection experiment.

Fig. 4.2: Images of chromosomes captured using an optical microscope.

4.2.2. Latex particle

Latex is a stable emulsion that consists of biopolimer microparticles dissolved in an aqeous medium. In this study, latex particles which were prepared by drying up the emulsion were used. The latex particle has the following characteristics.

- It has a morphology of pure sphere and its size (diameter) is known.
- It is constructed with biopolimer particles with relatively high density (1.03 g/cm^3). Also it is much thicker than the chromosome specimens. The high density and the large thickness of the latex particle prevent X-rays from penetrating through the specimens and allows high contrast imaging in comparison with the case for chromosome specimens which have far lower contrast than latex particle.

Therefore, projection images of latex particles were used in this study as a standard specimen based on its characteristics mentioned above. Effectiveness of the iteration procedure was compared between projection images of latex particles and those of chromosomes. Also, the effectiveness of the iteration procedure was also compared between different sizes (2 and 10 μmϕ) of latex particles. An example image of latex particles with 2 μmφ diameter captured by a scanning electron microscopy is shown in Fig. 4.2.
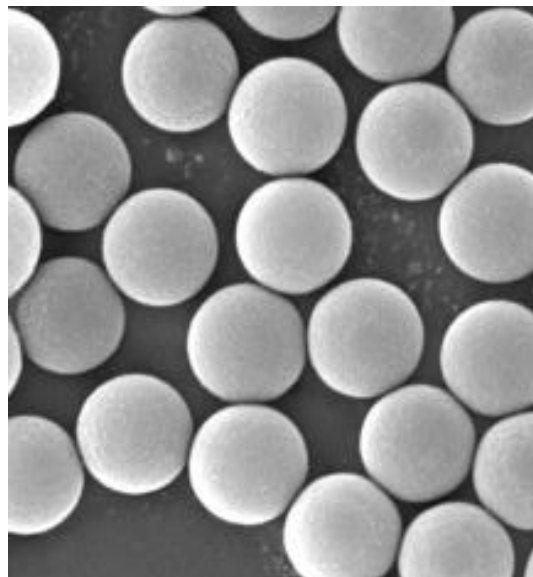
Fig. 4.3: Image of latex particle with 2 μmφ diameter captured using a scanning electron microscopy.

4.3. ITERATION PROCEDURE

Projection image of specimen captured with soft X-ray projection microscopy is blurred due to diffraction of X-rays. Then, spatial resolution of the specimen image is decreased due to influence of the blur. When phase and amplitude distributions of X-rays on CCD screen are known, blur correction is possible by using IFT calculation for inverse propagation of the X-rays to the specimen surface. The projection image has information about the amplitude distribution. However, we do not have any information about the phase. Thus the iteration procedure performs many repeated calculations of FT and IFT between the CCD screen and the specimen surface for the approximation of the X-ray phase distribution on the CCD screen. Finally a corrected specimen image is produced as a record of the X-ray intensity on the specimen surface. A diagram of the iteration procedure is shown in Fig. 4.4.
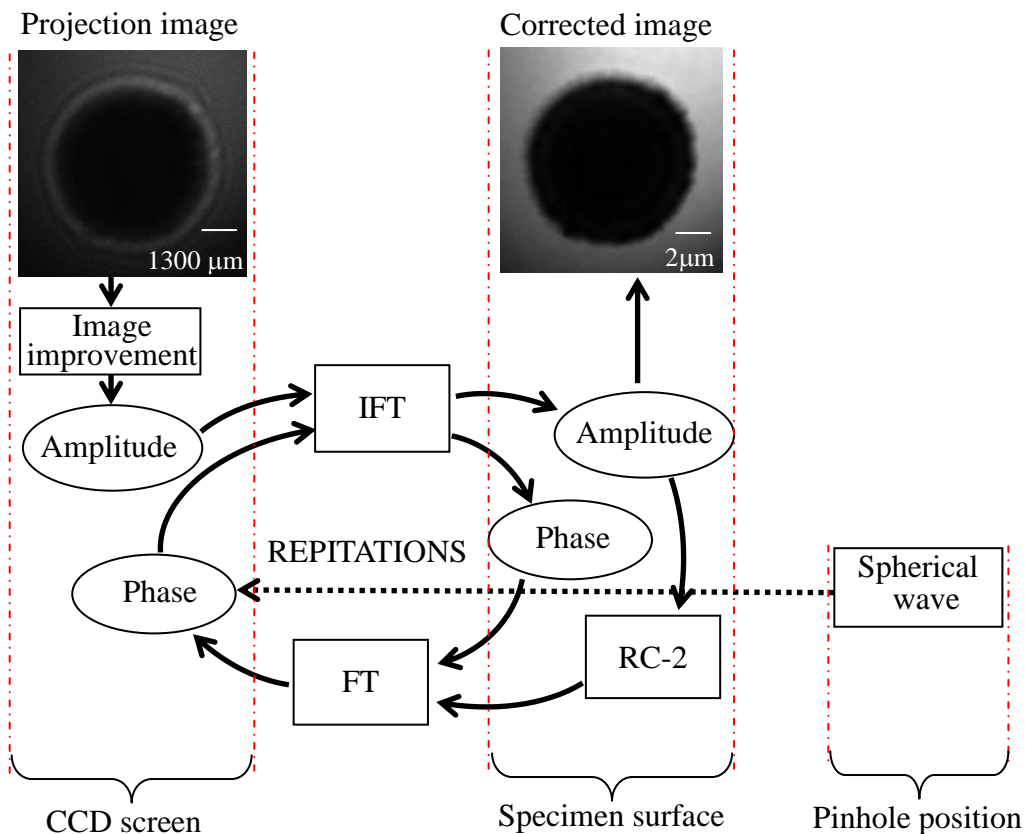
Fig. 4.4: Iteration procedure.
(Images: Latex particle with 10 μmφ diameter, magnification of 329 times, FT: Fourier Transformation, IFT: Inverse Fourier Transformation, RC-2: Restraint condition for amplitude distribution on specimen surface)

All steps of the iteration procedure shown in the diagram are explained as follows:

(1) Spherical wave which propagates from the pinhole to the CCD screen is calculated and phase distribution of the spherical wave is obtained as initail phase distribution of X-rays, because we do not have any information about the X-ray phase distribution which is essential for the correction of the experimental projection image.

(2) Noise removal and/or contrast enhancement is performed as image improvement for the projection image. Details of the image improvement method will be indroduced in the next section (4.4).

(3) Amplitude distribution on the CCD screen is obtained from the projection image after image improvement.

(4) The amplitude and the phase distributions are used for IFT calculation and an inverse propagation of the X-rays from the CCD screen to the specimen surface is calculated by the IFT. As a result, the amplitude and the phase distributions of the X-rays on the specimen surface are obtained.

(5) A restraint condition (RC-2) is used for the amplitude distribution on the specimen surface. Details of the RC-2 will be explained later.

(6) The phase and amplitude distributions on the specimen surface obtained from (4) and (5) steps are used for FT for calculation of the X-ray propagation from the specimen surface to the CCD screen. Then phase distribution of the X-rays on the CCD screen is obtained.

(7) (4)~(6) steps are repeated by using the estimated phase distribution in step (6) instead of the phase distribution of spherical wave in step (1). The repetition of the cycled calculations is stopped when the specimen boundary on the corrected image is not changed even if further calculation is carried out.

(8) Finally the corrected image is produced by calculating the intensity distribution of the X-rays from the amplitude distribution on the specimen surface.

Restraint condition for X-ray amplitude distribution on specimen surface

There is no reason why X-ray intensity on specimen surface becomes higher than the X-ray intensity at a situation without specimen (illumination intensity). Therefore, when the X-ray intensity on the specimen surface is higher than the illumination intensity, it is replaced with the illumination intensity. Fig. 4.5 shows the restraint condition.
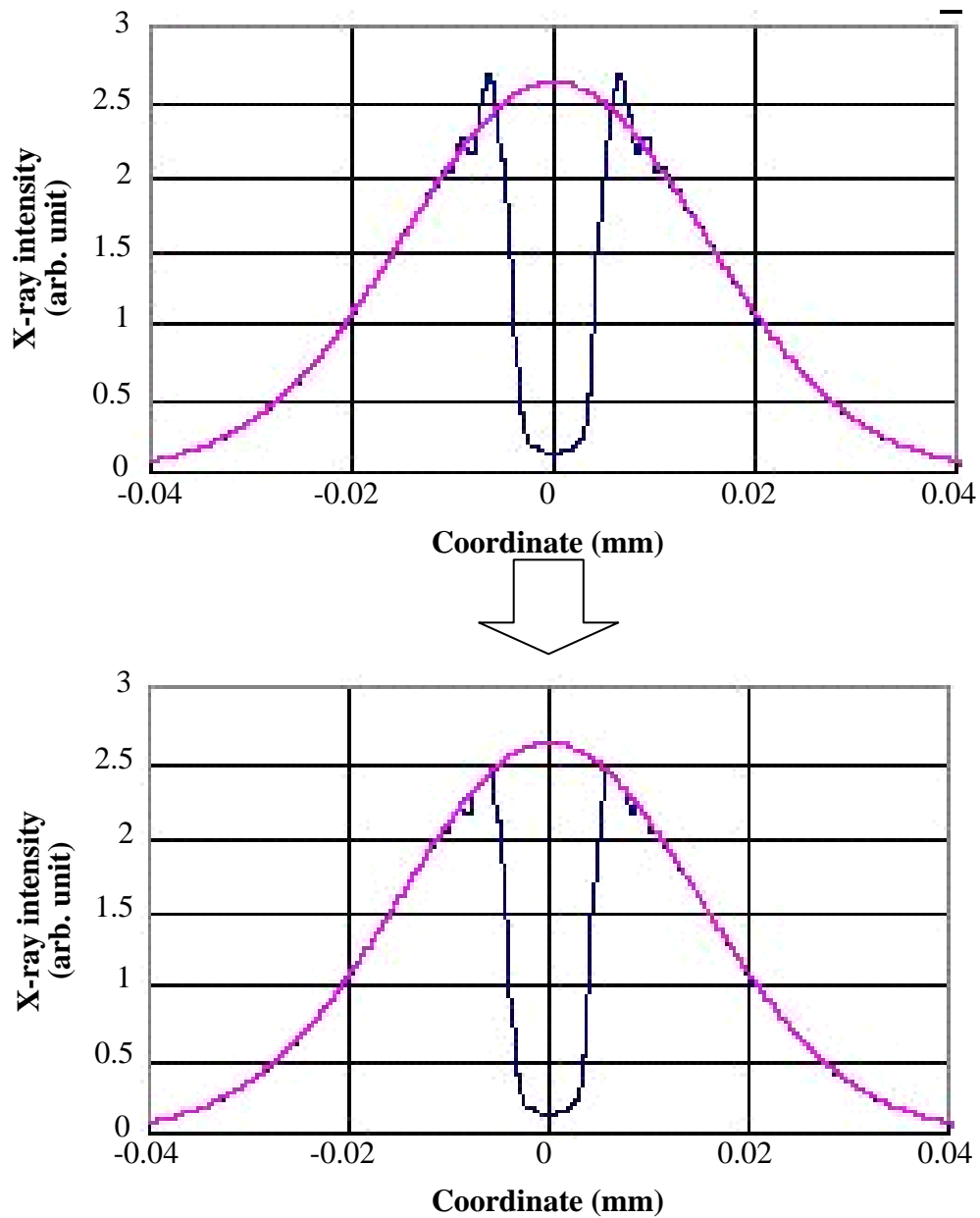
Fig. 4.5: Restraint condition.

The graphics in the top and the bottom sides of the figure are for the case before and after applying the restraint condition. Horizontal and vertical axes of the graphics are coordinate and X-ray intensity, respectively. The pink line shows illumination intensity whereas the black line shows the X-ray intensity on specimen surface.

Interpolation of sampling number

For the calculations of FT and IFT in the iteration procedure, the following two conditions of the number of samples are necessary:

- The numbers of samples on the specimen surface and on the CCD screen should be equal
- The number of samples should be defined as 2^n (n: positive integer) to use the FFT.

The pixel number of the projection image can be used as the sampling number on the CCD screen. However it is not applicable to the sampling number on the specimen surface due to the following restraint conditions of the sampling interval and the sampling region on the specimen surface. The sampling number is defined as the ratio of sampling region to sampling interval.

(1) Sampling interval on the specimen surface

Sampling interval on the specimen surface is calculated from sampling interval on the CCD screen by the equation (4.2) for a reversible relation between FT and IFT calculations.

$$T_0 = \frac{\lambda R}{L} \quad (4.2)$$

T_0 : Sampling interval on specimen surface

λ : Wavelength of the X-ray

R : Distance between the pinhole and the CCD screen

L : Sampling region on the CCD screen

The sampling region on the CCD screen is defined as the size of the projection image. Therefore the sampling region and the sampling interval on specimen surface should not be changed.

(2) The sampling region on the specimen surface

Since the sampling should be performed for the whole region of the specimen surface at least, the sampling region on the specimen surface should be equal or higher than the value calculated from the magnification of the imaging and the sampling region on the CCD screen by using equation (4.3).

$$L_0 = \frac{L}{X} \quad (4.3)$$

L_0 : Sampling region on specimen surface

L : Sampling region on the CCD screen

X : Magnification

Then, an interpolation for the number of samples is used depending on the projection conditions. The interpolation adjusts the number of the samples taking the restraint conditions (1) and (2) into account. An example of the interpolation for magnification of 166 times, distance between pinhole and CCD screen of 329 mm and wavelength of 1.77 nm is shown in Fig. 4.6.
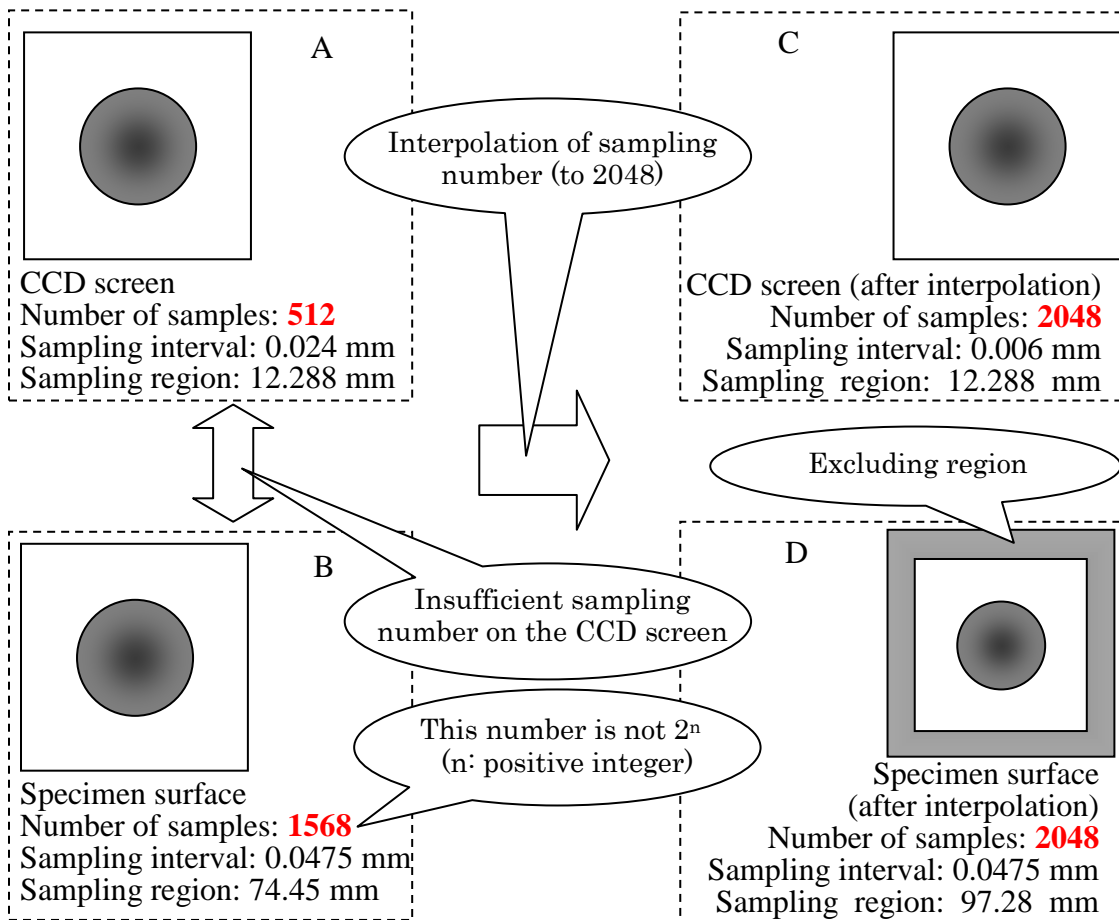
Fig. 4.6: Interpolation of sampling number.

In the panel A, sampling parameters on the CCD screen which were defined from region, pixel number and pixel pitch of the projection image are shown. In this case, the sampling parameters on the specimen surface were calculated by using the equation (4.2) and (4.3) (panel B). At least 1568 samples were necessary in this example. Therefore the number of sampling was interpolated to 2048 (2^{11}). Thus an excluding region is added to the image of specimen surface. The panel C and D show the results of interpolation to the CCD screen and the specimen surface, respectively.

The successfully corrected image should fulfill the following conditions:

(1) Contrast of the diffraction fringes against illumination intensity should be lower than 2% (A contrast criterion of the human eye's threshold, which could distinguish target contrast difference of 2% against the background intensity [42])

(2) The specimen boundary on the corrected image should show the chromosome morphology. The pixels of the specimen boundary of which contrast against illumination intensity is higher than 2% is traced and checked.

4.4. IMAGE IMPROVEMENT METHOD

The iteration procedure was not effective for all images, especially for the chromosome images whose diffraction fringes and/ or specimen morphology were not clear due to low contrast and high background noises for the images. An example of projection image of chromosome and its corrected result is shown in Fig. 4.7.
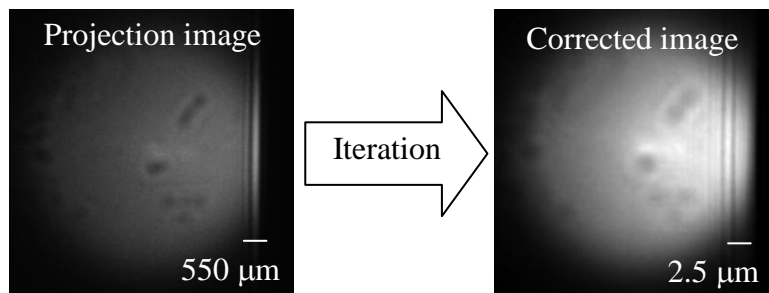
Fig. 4.7: Projection image and its corrected result for chromosome.
(Magnification: 219 times)

In this example, a bright fringe due to X-ray diffraction was captured around the specimen. However, the fringe remained on the corrected image. In other words, the iteration correction was not successful. For this projection image, contrast of the diffraction fringe was low and the background noise on the image was high compared with images that were correctable by the iteration procedure. An example of the images which were successfully corrected is shown in Fig. 4.8.
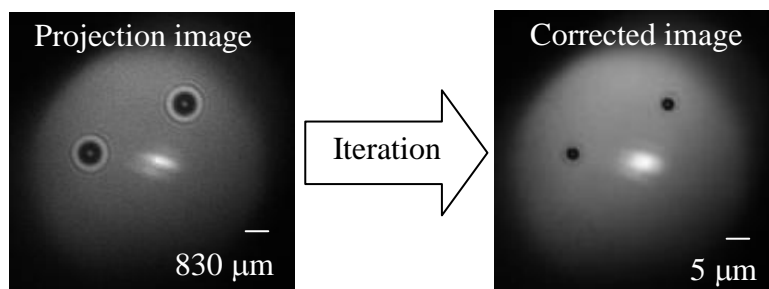
Fig. 4.8: Projection image and its corrected result for latex particle with 2.8 μm diameter.
(Magnification: 166 times)

In this projection image, two diffraction fringes were captured clearly around the specimen. Contrast of the innermost part was very high. However, contrast of the outermost part was not so high and was lower than or equal to the contrast of the

48

diffraction fringe of the chromosome image in Fig. 4.7. Nevertheless, the iteration procedure was highly effective in this case. It is considered that this successful correction depended mostly on the information of the innermost fringe. It may be concluded that at least one fringe of X-ray diffraction should be captured clearly for successful correction. Hence we developed an image improvement method prior to the iteration procedure, which consists of noise removal and contrast enhancement methods. For the evaluation and comparison of effectiveness of those methods, four processes with or without noise removal and/ or contrast enhancement methods could be considered as shown in Table 4.2.

Table 4.2: Image improvement prior to the iteration procedure.

-	Diagram[*]	Explanation
(1)		without noise removal and contrast enhancement
(2)		only contrast enhancement
(3)		only noise removal
(4)		noise removal and contrast enhancement

*: The process described with red lines (一) is active and corresponds to the
explanation in the right side (A: Noise removal, B: Contrast enhancement)

The details of the noise removal and contrast enhancement methods are explained in the next subsections (4.4.1 and 4.4.2). For the explanaitions, a schematic diagram of the projection image was applied. The model is shown in Fig. 4.9. In the center of a circular region representing the X-ray illumanation area, a specimen and diffraction fringes around the specimen are described. The noises are distributed randomly over whole area of the X-ray illumination.

In this study, the noise is defined as unnessessary parts of grayscale distributions on the projection image which break down the intensity distributions of the diffraction fringes, specimen and smooth illumination.

Fig. 4.9: Model of projection image.

4.4.1. Contrast enhancement

Intensity distribution of the X-rays on the CCD screen is recorded as the grayscale distribution of the projection image. In this case, a linear relation exists between the grayscale distribution and the intensity distribution of the X-rays, and this linearity should not be influenced by the contrast enhancement. Thus, a linear contrast enhancement method calculated by equation (4.4) [43] was used as a method which has no influence to the linearity.

$$G'(i, j) = \frac{G(i, j) - G_{min}}{G_{max} - G_{min}} \cdot G'_{max} \quad (4.4)$$

$G'(i, j)$: Grayscale value after the contrast enhancement for a pixel with coordinate (i, j).
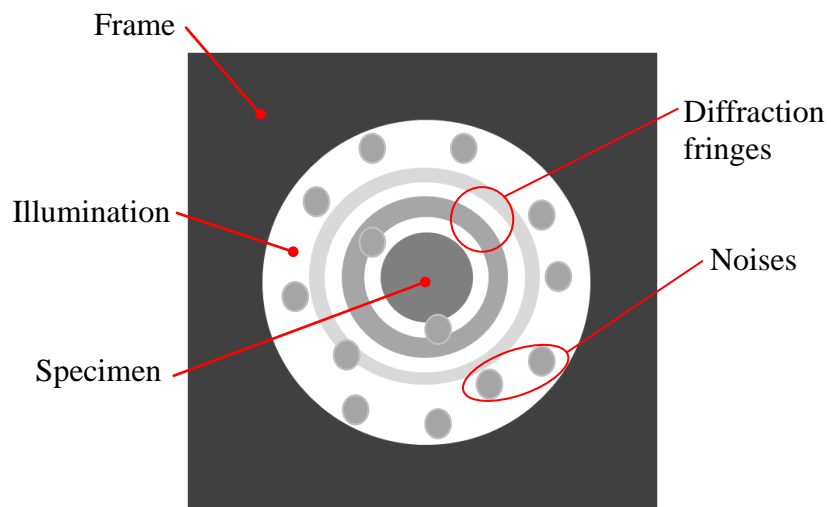
G'_{max}: Maximum value of the grayscale distribution on the image after the contrast enhancement

$G(i, j)$: Grayscale value before the contrast enhancement for a pixel with coordinate (i, j).

G_{max}: Maximum value of the grayscale distribution on the image before the contrast enhancement

G_{min}: Minimum value of the grayscale distribution on the image before the contrast enhancement

When applying the linear contrast enhancement method, minimum and maximum values of the original grayscale distribution on the projection image are assigned to a new set of values. Therefore, the full range of available grayscale values can be utilized. In Fig. 4.10, the same model of projection image as in Fig. 4.9 except background noises is also shown. A broken line with red color is a cross-sectional line that refers to the grayscale distribution in Fig. 4.11. Two models for the grayscale distributions on a cross-sectional line of the model projection image before and after the contrast enhancement were illustrated in the figure (blue and red broken lines). In this model, the intensity difference of diffraction fringe as shown by blue double arrows could be enhanced about twice as described by the red double arrows on the figure.

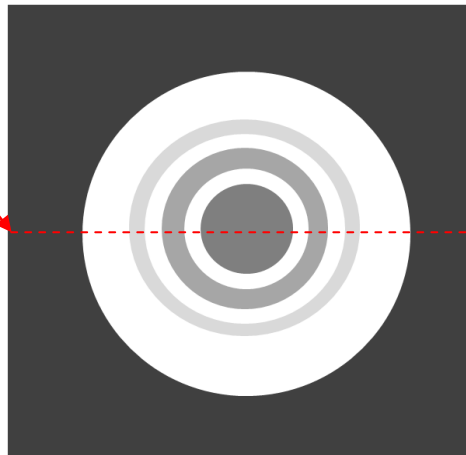A cross sectional line for grayscale distribution in a graphic of Fig. 4.11
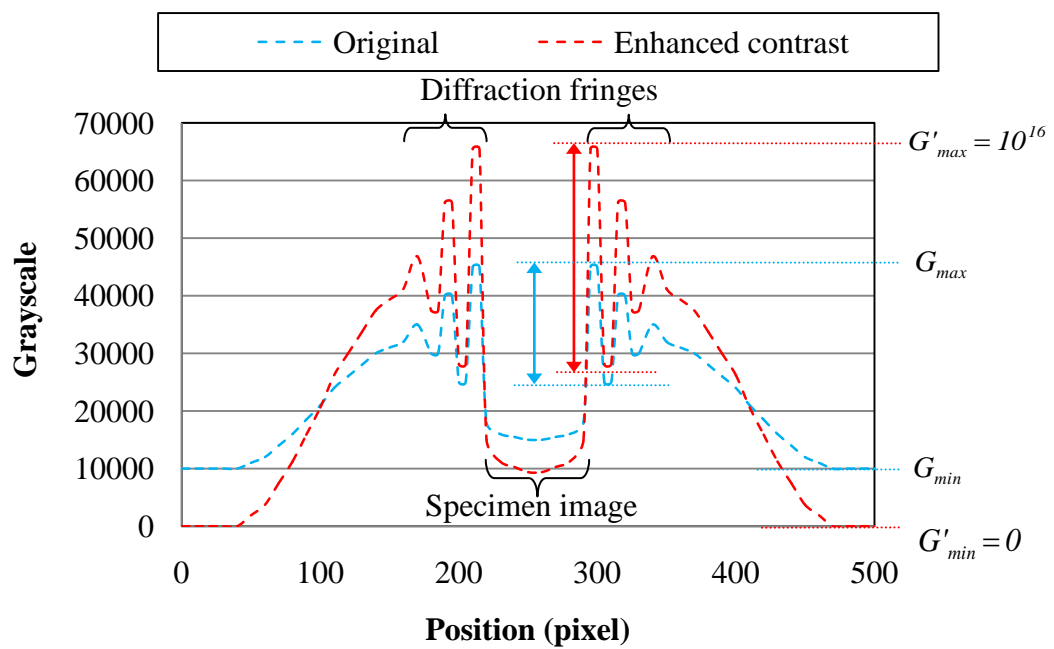
Fig. 4.10: Model of projection image.

Fig. 4.11: Grayscale models before and after contrast enhancement.

52

4.4.2. Noise removal

In general, a median filter and a moving average methods are applied as non linear noise removal method for the background noises which were randomly distributed through the whole area of the image. While all edges on the image become obscure by the moving average method, the noise removal is possible without any influence to the image edges by the median filter method. Since the projection images captured by our projection experiment contain some important informations about specimen image and diffraction firnges, we chose the median filter method to remove the background noises on the projection image.

In the median filter, the following process is performed for each pixel of the image. At first, the method selects N x N pixel region and arranges the grayscale values of the selected pixels. Then the grayscale value of the pixel at the center of selected pixel regions is replaced with a median value of the arranged grayscales. Algorithm of the median filter (An example with 3 x 3 pixel region) is shown in Fig. 4.12 [44].
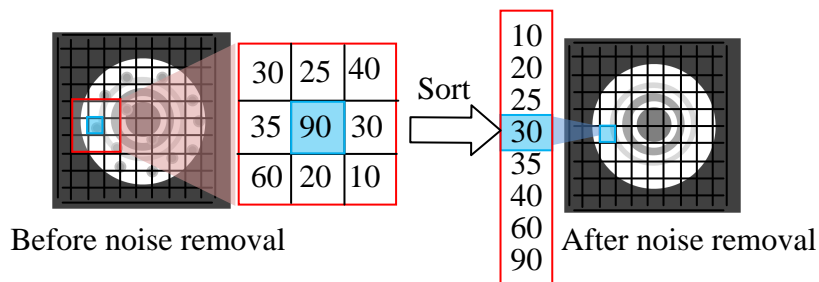
Fig. 4.12: Algorithm of noise removal by median filter.

In this example, the grayscale value of a pixel with noise (90) was removed by replacing with the median value (30) of the selected regions. Any size of the pixel region is possible for this median filter. However, the median filter with 3 x 3 pixel region was applied for this study.

Background noise on the projection image has a different property from that of the diffraction fringes, and the specimen image recorded on only one or a few pixels. Therefore it is possible to remove most of the noise by the median filter with the smallest pixel region (3 x 3). On the other hand, it might induce a loss to the diffraction fringes and the specimen image by the median filter with larger region of pixels. A model of grayscale distributions for specimen image and background noises before and after noise removal is shown in Fig. 4.13. Fig. 4.13 (a) and (b) show grayscale distributions of the pixel regions with different sizes estimated by the median filter. In this case, comparison was made for 3 x 3 and 5 x 5 pixel regions. The horizontal and

vertical axes are pixel and grayscale distribution, respectively. For the region of 3 x 3 pixels, the medean filter could remove the background noises without influencing the grayscale distribution of the specimen. However, position of the grayscale boundary for the specimen was deviated for the region of 5 x 5 pixels.
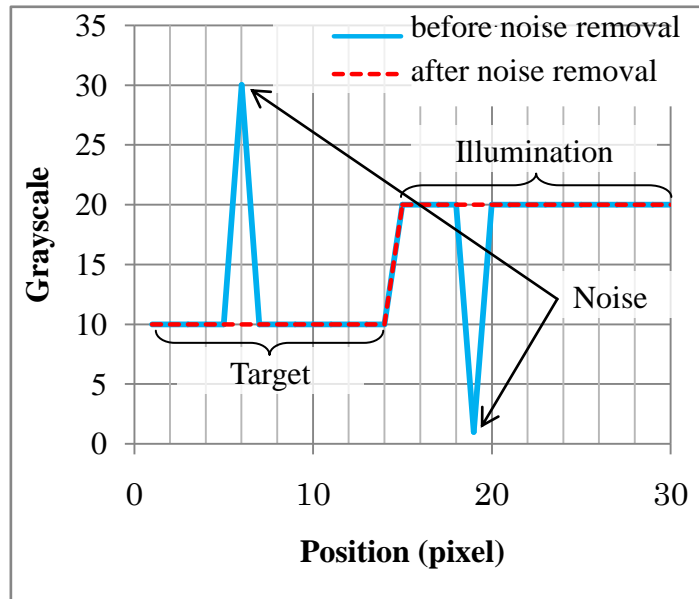
(a) Pixel region for median filter: 3x3
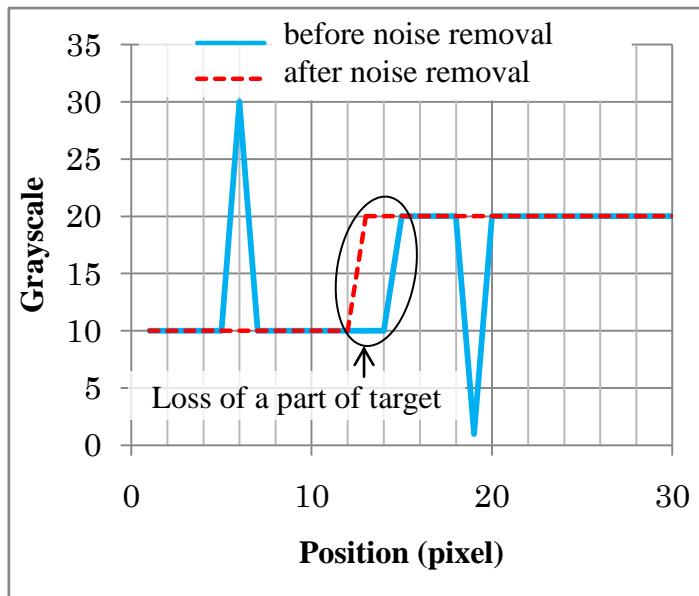
(b) Pixel region for median filter: 5x5

Fig. 4.13: Grayscale distributions on a model for a part of projection image before and after the noise removal. (Comparison of noise removal effectiveness in the cases of 3x3 and 5x5 pixel regions for the median filter)

4.5. SIMULATION OF PROJECTION IMAGE

In order to evaluate the limits of the background noise on the projection image where the iteration procedure can work effectively, a simulation study was performed. In the simulation study, we prepared a model specimen of known morphology with the background illumination of X-rays which was obtained experimentally, because the critical factor which affects the iteration calculation and results in lowering the spatial resolution is supposed to be the spatial variation of X-ray illumination. Therefore, the correction of the illumination variation has been a main issue in our imaging experiments. The process is shown in Fig. 4.14.
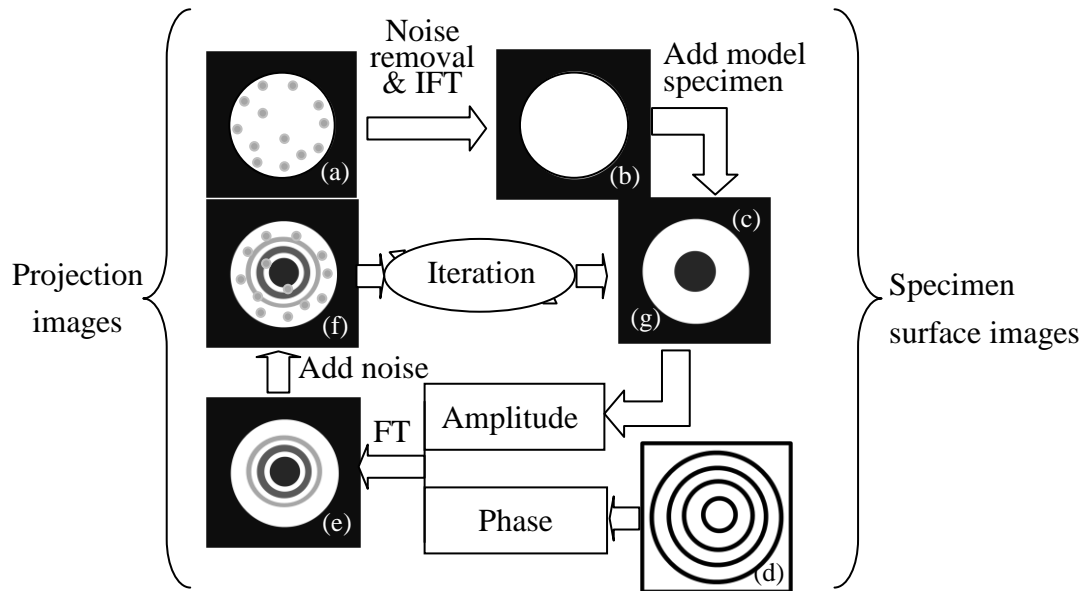
Fig. 4.14: Simulation and correction procedure for the projection image.
(a) X-ray image of illumination by experiment, (b) X-ray image of illumination for simulation, (c) Specimen image, (d) Phase distribution of spherical wave, (e) Projection image without noise, (f) Projection image with noise, (g) Corrected image

At first an X-ray image of illumination was captured experimentally (a), and the image for simulation on the specimen surface (b) was obtained by removing the background noise with a simple moving average process and by applying IFT on the image (a). Then the specimen image (c) was prepared by adding a model specimen on the image (b).

Projection image (e) was calculated using FT. The calculation used amplitude distribution from the specimen image (c) and the phase distribution of spherical wave on the specimen surface (d), because X-ray spherical wave was used for projection experiments. Then artificial noises were added to the projection image (e) directly for evaluation of the noise influence, leading to the projection image (f). The noise distribution was set up randomly, and the sizes and the number of noise were based on the noise information of experimental projection images, where the blur correction by the iteration procedure was not effective. Noise contrast, defined as a ratio of the difference between the highest and lowest value of intensity for the noise to the illumination intensity, was introduced as variables.

To correct the projection image (f), the iteration procedure was applied to the X-ray intensity distribution on the specimen surface of the opposite side of the X-ray source.

The noise contrast divided by the contrast of diffraction fringe, which was defined below, was adopted to evaluate the noise for the chromosome image with relatively high contrast, because some of the images with relatively high contrast were successfully corrected by adjusting the contrast of noise and diffraction fringes. Therefore the ratio of the noise contrast to the contrast of diffraction fringes was considered as a good measure of noise in this case. The contrast of the diffraction fringes was defined similarly to the noise contrast as a ratio of the difference between the highest and lowest values of intensity for the diffraction fringes to the illumination intensity. A relationship between the contrast ratio in the projection image (f) and contrast of the diffraction fringes in the corrected image (g) was examined, because the problem in this case was that the diffraction fringes remained in the corrected image.

On the other hand, the relationship between contrast of the target in the corrected image (g) and noise MSE (Mean Squared Error) [45, 46] of the projection image (f) was studied for the chromosome image with very low contrast where the diffraction fringes were hardly detected and the contrast of target (specimen morphology) was lost by the iteration procedure. The noise MSE was adopted to evaluate the noise by taking all the parameters of the noise (noise number, size and contrast) into account, because the images were not correctable even if the contrast enhancement was performed prior to the iteration procedure while some images with relatively high contrast were corrected effectively. The noise MSE was defined using equation (4.5) as a value of square grayscale per pixel [45].

$$MSE = \frac{1}{N} \sum_{n\_1}^{N} \left(G_n - G_n^0 \right)^2 \quad (4.5)$$

G_n : Grayscale value of n in a pixel of the projection image with

noise (panel f)

G_n^0 : Grayscale value of n in a pixel of the projection image without

noise (panel e)

N : Total number of the image pixels (=512*512)

To evaluate the contrast of the target, we chose "equation (4.6)" based on the "Weber diffraction definition of contrast [47]".

$$Contrast = \frac{|G_1 - G_2|}{G_{max}} \quad (4.6)$$

G_1 : An average value of the grayscale distribution around the target in an area between the large square and the small square

G_2 : An average value of the grayscale distributions on the target in the small square

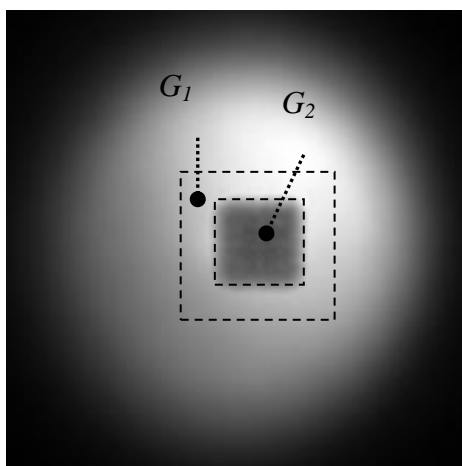G_{max} (= 2^{16}): 16 bit depth, is maximum value of the grayscale (Fig. 4.15)

Fig. 4.15: Area selections for contrast evaluation of specimen image.

CHAPTER 5: RESULTS AND DISCUSSION

5.1. EFFECTIVENESS OF ITERATION PROCEDURE

Effectiveness of the iteration procedure was tested on projection images of chromosome and latex particles with 2 and 10 μm diameters. The projection images were captured at the magnification of 47 ~ 658 times and the effectiveness of the iteration procedure is summarized in Table 5.1, which depends on the magnification.

Table 5.1: Effectiveness of iteration procedure.

Specimen	Magnification (times)						
	low					high	
	47	66	165	219	329	504	658
Chromosome	3.3	3.1	3.9	4.0	3.4	X	X
Latex particle (2 μm)	0.1	0.0	0.2	0.0	0.0		0.0
Latex particle (10 μm)	0.2	0.3	0.2	23.5	21.2		18.5

*1) The numbers in the red rectangle show the contrast of diffraction fringes (%).

*2) Gray highlights: the corrected images fulfilled the condition of successful correction, which the contrast of diffraction fringes is below 2%.

*3) X: excluded (diffraction fringes in the projection images were not observable. Some or the whole parts of the target were lost by the iteration procedure)

As shown in Table 5.1, the following results were obtained.

(1) All images were not correctable for chromosome. Representative examples of projection images of the chromosome and its corrected results are shown in Fig. 5.1. For the images with high magnifications of 504 times or more, the contrast of projection images was very low, which was frequently experienced in the case of chromosomes and the diffraction fringes were hardly detected. In this case the corrected images should be the same as the projection images. In other

words, the morphology of the projection image should not be changed by the iteration procedure. However some or the whole part of the specimen image were lost by the iteration procedure as shown in Fig. 5.1 (a).

For the images with 329 times magnifications or lower, diffraction fringes remained on the images after the iteration correction even in the situation where diffraction fringes were observable on the projection images. The contrast of the diffraction fringes in the corrected images was 3%~4% which is obviously higher than the contrast criterion (2%). In order to show the diffraction fringes clearer, grayscale distributions on the cross-sectional lines of the images in Fig. 5.1 (b) are shown in Fig. 5.2. Broken lines with black color show the diffraction fringes.

(2) All images of a latex particle with 2 μm diameter were corrected successfully. A representative example of the projection and corrected images is shown in Fig. 5.3. In the successfully corrected images, the diffraction fringes disappeared and the contrast of the diffraction fringes was examined to be 0%. The particle size (the specimen boundary which was traced on the corrected image) was equal to the estimated value of its size.

(3) Some images of the latex particle with 10 μm diameter with 165 times magnifiaction or lower were corrected successfully. However, the effectiveness of the iteration procedure was not enough for images with magnification of 219 times or more. Representative examples of the images for successful and insufficient corrections are shown in Fig. 5.4 (a) and (b), respectively. For the images with insufficient correction (b), diffraction fringes remained after the iteration procedure and contrast of the innermost diffraction fringes was about 20%. On the other hand, the diffraction fringes disappeared and the contrast of the diffraction fringes was calculated to be 0%. The particle size (the specimen boundary which was traced on the corrected image) was equal with an estimated value of its size for the images with successful correction (a).
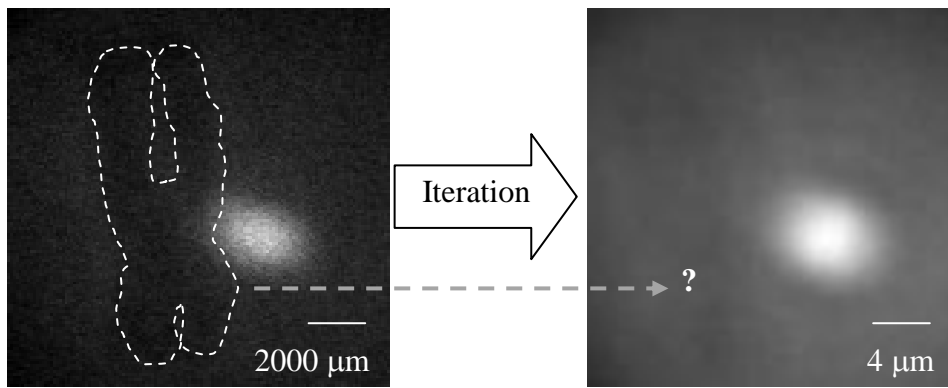
(a) Magnification: 504 times
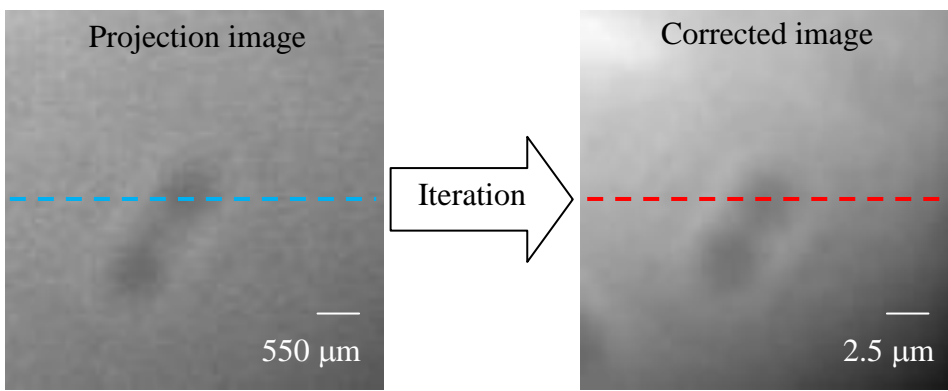
(b) Magnification: 219 times

Fig. 5.1: Representative examples of projection and corrected images of chromosome.
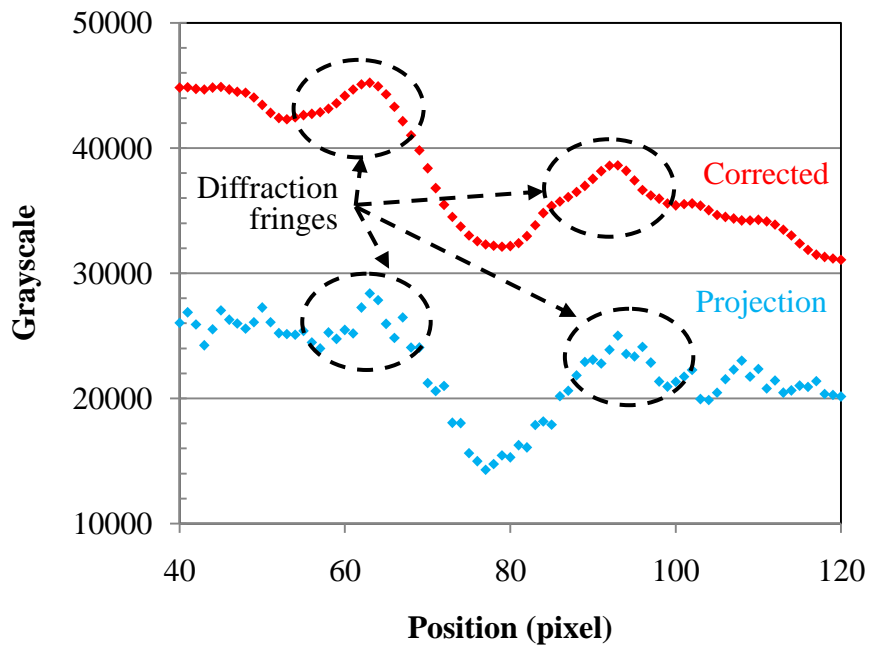
Fig. 5.2: Grayscale distribution on a cross-sectional line of chromosome image with magnification of 219 times.

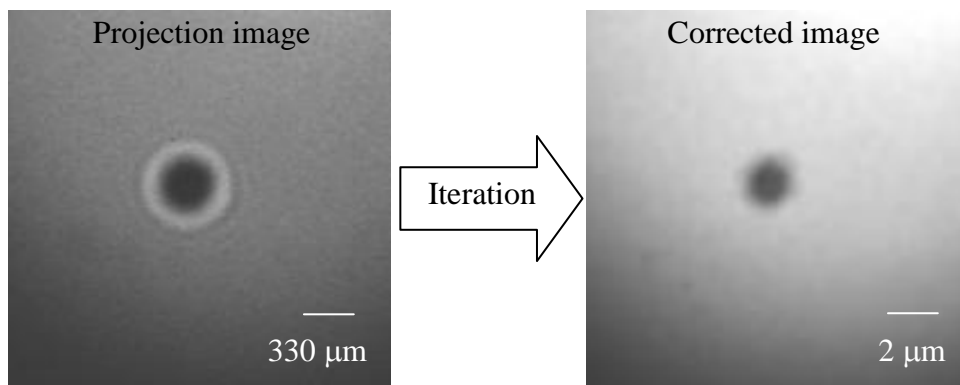(The red and blue expressions correspond to the lines in Fig. 5.1 (a), respectively)

Fig. 5.3: Representative example of projection and corrected images of latex particle with 2 μm diameter (Magnification: 165 times).
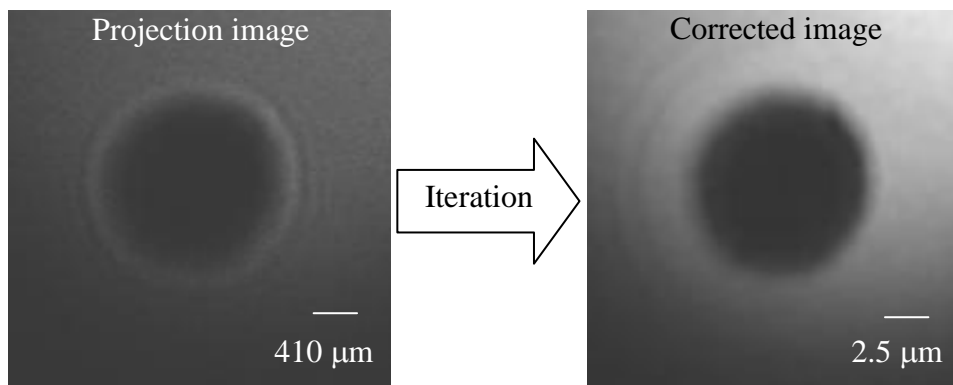
(a) Example of successful correction (Magnification: 165 times).
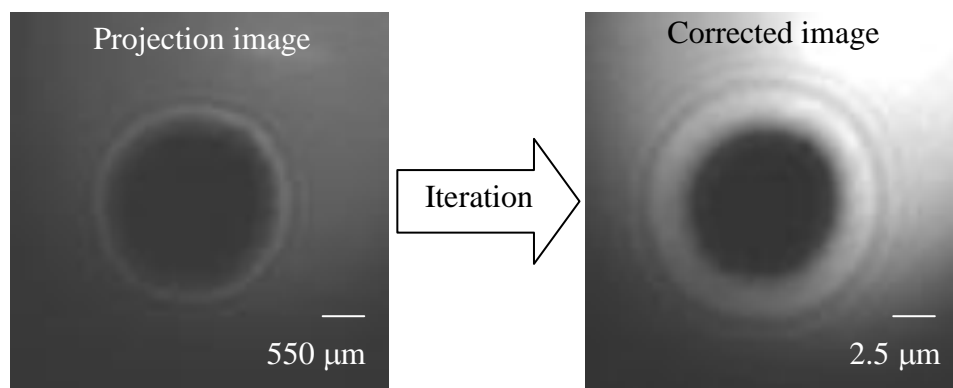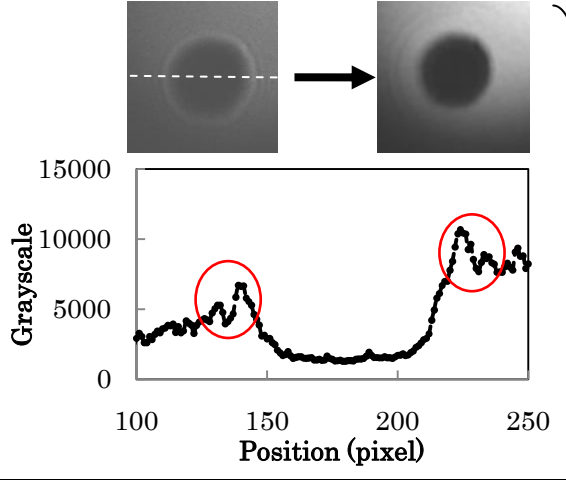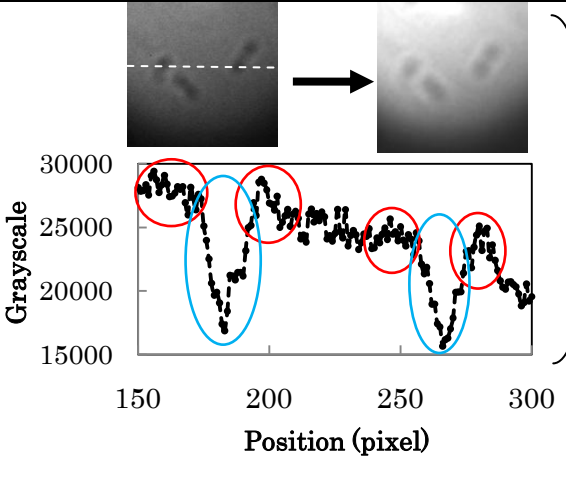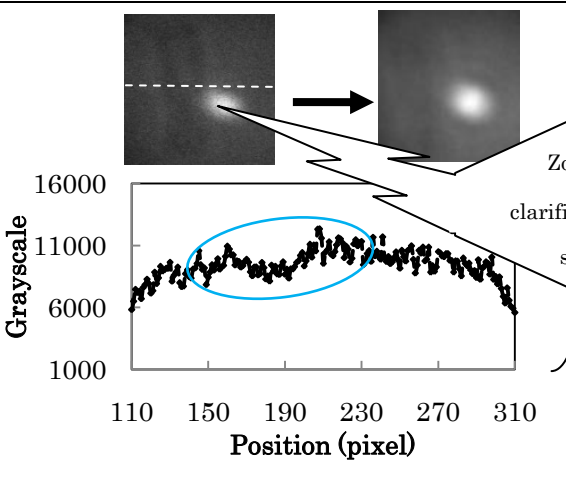
(b) Example of insufficient correction (Magnification: 219 times).

Fig. 5.4: Representative example of successful and insufficient correction for projection images of latex particle with 10 μm diameter.

In considering the cause and finding the solution for the insufficient correction in the chromosome images, we have analyzed the grayscale distributions on the projection images. The grayscale distributions on the chromsome images were compared with the projection images of the latex particle which were successfully corrected by the iteration procedure. The grayscale values of the images with high and low magnifications were also compared. Representative example for the comparison of grayscale distributions is shown in Table 5.2.

Table 5.2: Comparison of grayscale distributions on projection images.

Latex particle (φ10 μm)	(Magnification: 165 times)	Grayscale vs Position (pixel): 100–250, Grayscale 0–15000	○: Diffraction fringe The projection image of the chromosome had the following differences when compared with the image of the latex particle ・Background noise is high ・Contrast of the diffraction fringes is low	
Chromosome		Grayscale vs Position (pixel): 150–300, Grayscale 15000–30000	○: Specimen Contrast of the specimen image was very low for the image with high magnification	
	(Magnification: 504 times)	Grayscale vs Position (pixel): 110–310, Grayscale 1000–16000	Zoom up & clarification of specimen 2000 μm	

➡ : Iteration procedure

In the table, projection images and their corrected images of the latex particle with 10 μm diameter, chromosomes with different magnifications and their grayscale distributions on cross sectional lines on the projection images are shown.

For the chromosome images, background noise was very high compared with that of the latex image. The noise may mainly come from scattering X-rays from debris of fragmented intracellular components around the chromosome specimen and from the chromosome itself, since the chromosome specimen is structurally heterogeneous compared with the latex particles. Therefore for the chromosome images with low magnification and relatively high contrast, the X-ray diffraction fringes were considered to be interrupted by the background noise, resulting in difficulty in identifying the diffraction fringes in the iteration procedure.

For the high magnification images, contrast of the target was very low. Consequently the specimen image disappeared after the iteration procedure due to the high background noise in addition to its too low contrast. Totally low signal to noise ratio may result from the fact that X-rays were shielded largely by the specimen resulting in decrease in image contrast due to the decrease of the X-ray intensity on the CCD screen. For the high magnification imaging, specimen should be placed close to the point source (pinhole). Increase in the scattering X-rays and background noise due to high illumination intensity on the specimen surface should be considered for the high magnification imaging.

Also for the low correction effectiveness on the high magnification images of large latex particle, the same reasons i.e. high background noise and low image contrast which leads to low contrast of diffraction fringes and poor iteration effectiveness are considered.

Therefore we tried to enhance the image contrast for the specimen and the diffraction fringes prior to the iteration procedure. An image improvement method consisting of contrast enhancement and noise removal methods were tried. The results are introduced in next section (Section 5.2).

5.2. EFFECTIVENESS OF IMAGE IMPROVEMENT PRIOR TO ITERATION PROCEDURE

Effectiveness of the image improvement method as mentioned in the section 4.4 was evaluated on the projection images of the latex particles with 10 μm diameter and chromosomes. In the image improvement, noise removal and contrast enhancement methods were used in individually or in a combination of them. The results are summarized in Table 5.3.

Table 5.3: Effectiveness of the iteration procedure with or without image improvement.

—		Magnification (times)						
		low					high	
		47	66	165	219	329	504	658
A→C (only C)	Latex particle (10 μm)	0.2	0.3	0.2	23.5	21.2	/	18.5
	Chromosome	3.3	3.1	3.9	4.0	3.4	X	X
B→C	Latex particle (10 μm)	0.0	0.0	0.1	0.2	20.2	/	19.0
	Chromosome	0.0	0.2	0.4	0.4	3.3	X	X
A→B→C	Latex particle (10 μm)	0.0	0.0	0.1	0.0	0.0	/	0.0
	Chromosome	0.0	0.2	0.3	0.2	0.4	X	X

*1) A: noise removal, B: contrast enhancement, C: iteration procedure

*2) The numbers in the red rectangle show the contrast of diffraction fringes (%).

*3) Gray highlights: the corrected images fulfilled the condition of successful correction which the contrast of diffraction fringes is below 2%.

*4) X: excluded (diffraction fringes in the projection images were not observable. Some or whole parts of the target were lost by the iteration procedure)
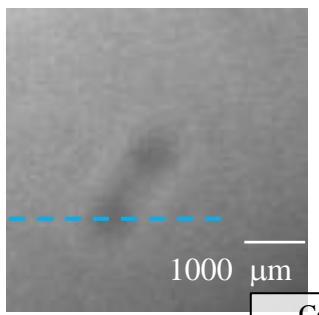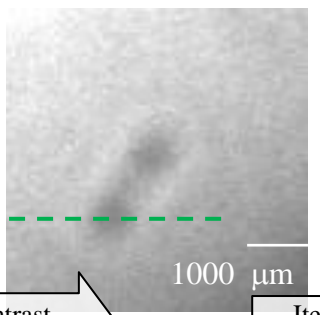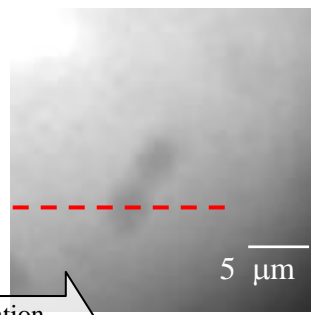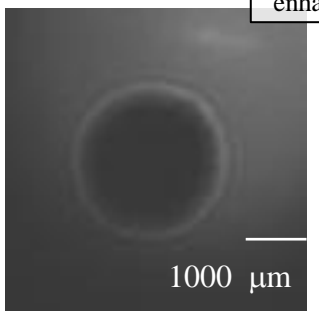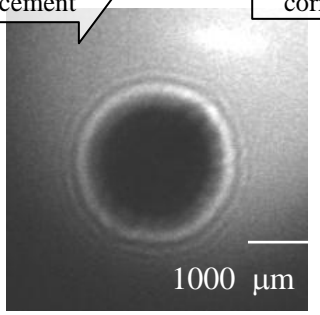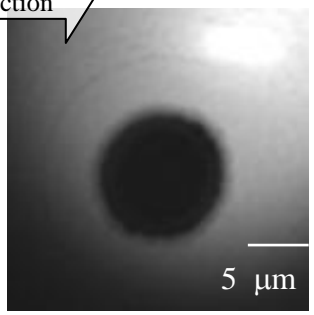
Successful corrections were shown by the gray highlights in the table. Contrast of diffraction fringes in the successfully corrected images was obtained to be almost 0%. On the other hand, the contrast of the innermost diffraction fringes was about 20% for the images of latex particle with insufficient correction. The contrast of the diffraction fringe was 3%~4% for the chromosome images with insufficient correction except the images with high magnification (504 times or more). The chromosome images with
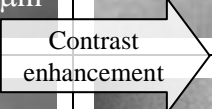
high magnification were lost by the iteration procedure and its morphology was not observable in the corrected images.

In the beginning of this study, effectiveness of iteration procedure was evaluated on the images from which background noise was removed. However, the result was the same as the case where the background noise was not removed.

Contrast enhancement prior to the iteration procedure provided successful correction for the images with magnification of 219 times or lower. A representative example for the effectiveness of the contrast enhancement method is shown in Table 5.4. In the table, projection (with and without contrast enhancement) and corrected images of chromosome and latex particle with magnification of 219 times were shown as examples, which were not correctable solely by the iteration procedure and corrected effectively after the contrast enhancement. Grayscale distributions on cross-sectional lines of the chromosome images are shown in Fig. 5.5 for the confirmation of the diffraction fringes.

Table 5.4: Representative images for effectiveness of contrast enhancement method (Magnification: 219 times).
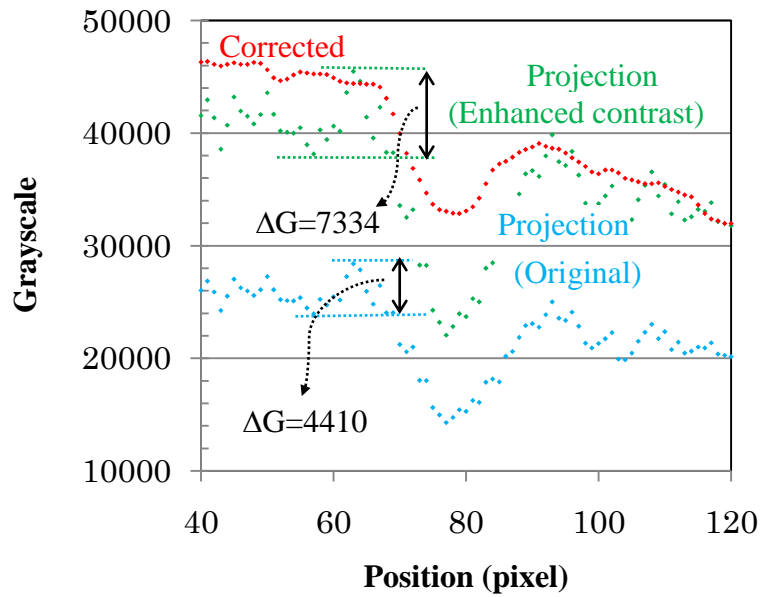
Fig. 5.5: Grayscale distribution on a line of chromosome image.

Horizontal and vertical axes show position on the lines and grayscale value, respectively. Blue, green and red graphs correspond to the broken lines on the projection images without and with contrast enhancement and corrected image.

The contrast enhancement method was effective especially for the correction of the chromosome images which are not correctable solely by iteration procedure. The results suggested that sharpening and deepening the image contrast made enough difference for the iteration correction between the contrast of diffraction fringes and background grayscale distributions. In the case of chromosome image shown in Table 5.5, the diffraction fringe contrast was enhanced by about 1.7 times as described in the blue and green curves on Fig. 5.5.

Finally, effectiveness of the iteration procedure with contrast enhancement was also evaluated after applying the noise removal method. The correction effectiveness became even better and all images of the latex particle and images of the chromosome with 329 times magnification or lower were corrected successfully. Projection images before and after noise removal, and correction results by the iteration procedure with contrast enhancement are shown in Fig. 5.6. Grayscale distributions on the cross sectional lines of these images are also shown in graphics of Fig. 5.7 for the confirmation of the noise removal effectiveness and the correction effectiveness of the diffraction fringes.
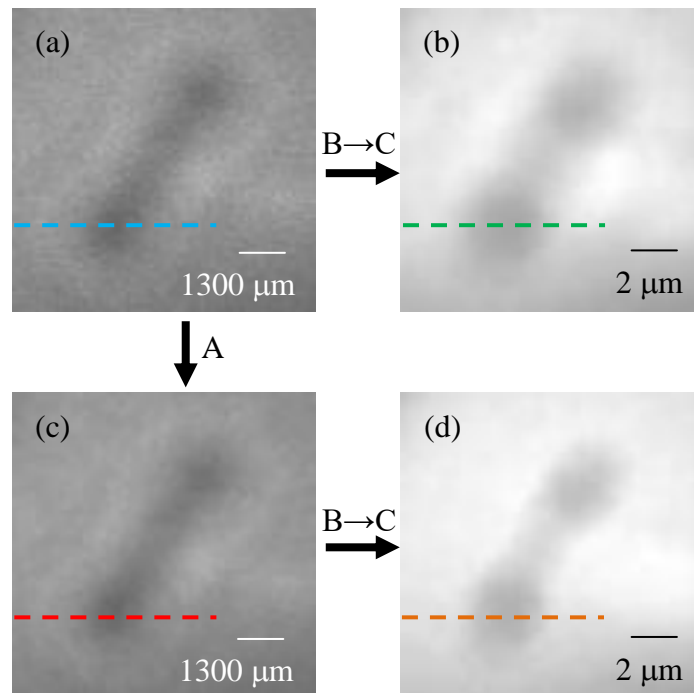
Fig. 5.6: A representative example of the iteration correction for the chromosome image with low magnification (Magnification: 329 times).
(a) Projection image (without noise removal), (b) Corrected image (without noise removal), (c) Projection image (with noise removal), (d) Corrected image (with noise removal), A: Noise removal, B: Contrast enhancement, C: Iteration procedure
Broken lines (− −) correspond to the grayscale distributions described in Fig.5.7.
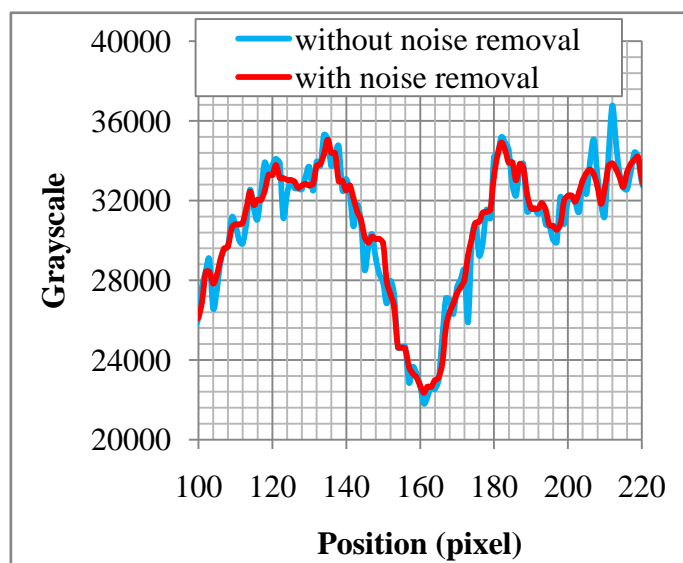
(a) for the projection images
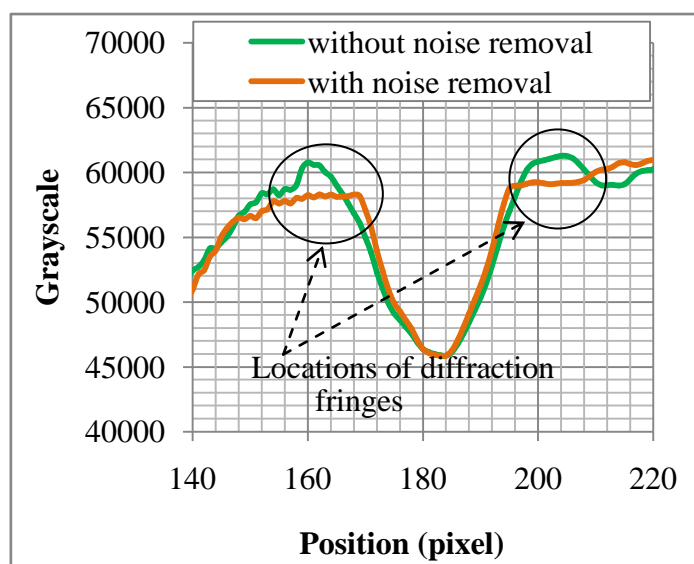
(b) for the corrected images

Fig. 5.7: Comparison of grayscale distributions on a line of projection and corrected images with and without noise removal. (The images are shown in Fig. 5.3)

Horizontal and vertical axes of the graphics are position on the lines and grayscale distribution, respectively.

By the noise removal method, the background noise on the projection image was removed effectively but not completely. Fig. 5.7 (a) shows the grayscale distribution of the projection images before and after the noise removal. The blue and red lines of the graphic correspond to broken lines on the images in Fig 5.6 (a) and (c), respectively. By

applying noise removal, the iteration procedure with contrast enhancement could correct some images which were not correctable before. Fig. 5.7 (b) shows the grayscale distribution of the corrected images. The green and orange lines correspond to broken lines on the images in Fig 5.6 (b) and (d), respectively. The diffraction fringes on the corrected image disappeared in the case with noise removal. Conversely the diffraction fringes remained on the corrected image in the case without noise removal as shown in black curves on the figure.

We have continued to investigate on how to further improve the correction effectiveness. One candidate for the improvement was to evaluate the upper limit of background noise. The evaluation of the upper limit of background noise for the effective correction was attempted on a simulation study. The result was compared with the noise removal effectiveness of the median filter method. Details of the result are described in the next section (Section 5.6). A simple and effective washing of the specimen using fresh fixative has been also adopted to clean up the debris with few loss of chromosomes. The effectiveness of washing specimens will be evaluated in the next study.

5.3. EVALUATION OF NOISE LIMITS

The following two simulation studies were separately executed for the chromosome images with relatively high contrast or with very low contrast.

(1) Iteration effect for the chromosome image with relatively high contrast:

The noise contrast was changed from 0 to the equal level with the contrast of the diffraction fringes for the simulated projection image. The ratio of the noise contrast to the contrast of the diffraction fringes, abbreviated as "ratio K" in the following text, is introduced. The iteration effect was examined for each level of the noise contrast in Figs. 5.8 to 5.10. Below 0.95 of the ratio K, the correction was found to be successful. Therefore the upper limit for successful correction was determined as 0.95. Image examples at each step in the simulation and the iteration procedures are shown in Fig. 5.8. The images in Fig. 5.8 correspond to those in Fig. 4.12 with same numbers (a ~ g). The X-ray illumination image (a) was captured by a projection experiment and the simulation conditions were adjusted to be the same as the projection experiment at the magnification of 329 times. The magnification was calculated as the ratio of distances from pinhole to CCD screen and to specimen position based on its optical layout. The size of the square for specimen (c) was 4 μm * 4 μm. The ratio K was adjusted to 0.95 or 1.00 in the projection images (f-1) and (f-2), respectively.

   In order to show the correction effectiveness more clearly, a comparison between grayscale distributions of Fig. 5.8(g-1) and (g-2) is shown in Fig. 5.9A and Fig. 5.9B. The vertical axis is the difference between grayscale distributions on cross-sectional lines of the corrected image in Fig. 5.8(g-1) or (g-2) and the X-ray image of illumination (b). The horizontal axis is the pixel position. Zoomed-up images of four edge areas on the grayscale profiles in corrected specimen images indicated by rectangles with broken lines were also shown in Fig. 5.9. The diffraction fringes remained in the corrected image and the edge of the specimen image was not clear in the case when the contrast was almost equal between noise and diffraction fringe (the ratio K of 1.00, Fig. 5.9B). On the other hand, by lowering the ratio K by 0.05, the correction was greatly improved where the diffraction fringes were removed and the specimen edge was corrected clearly (Fig. 5.9A).

   A relationship between the ratio K and the contrast of the diffraction fringes in the corrected image is shown in Fig. 5.10. The criterion of the contrast of the diffraction fringes in the corrected image whether the correction is successful or not (2%) was described by the horizontal broken line. "O" and "X" characters show correctable and

uncorrectable region of the ratio K, respectively.

In the successfully corrected images with the ratio K of 0.95 or lower, contrast of the diffraction fringes in the corrected image was lower than 0.5% (Fig. 5.10) and the diffraction fringes disappeared. Traced line of the specimen boundary was also equivalent to that of the model specimen for all corrected images in these cases. On the other hand, diffraction fringes remained in the corrected image where the ratio K exceeded 0.95. The contrast of the diffraction fringes in the corrected image was in the range between 2% and 3.5%. A blurred part is still visible in the image despite of correction. In the case where the correction was insufficient, the X-ray diffraction fringes were considered to be interrupted by the noises with the ratio K higher than 0.95, resulting in inability to identify the diffraction fringes in the iteration procedure.

The results suggested that the diffraction fringes accompanied with the experimental projection image of chromosome would be corrected effectively by the iteration procedure when the ratio K is lower than 0.95 of the diffraction fringe contrast.
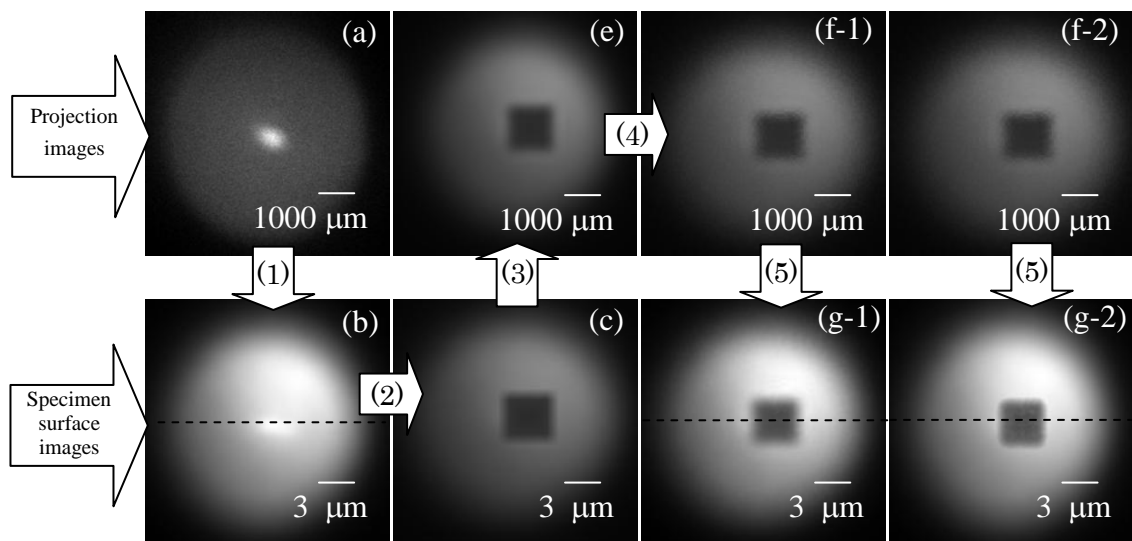
Fig. 5.8: Representative results of the iteration effect on a model specimen image with high contrast.

(a) X-ray illumination image in the experiments, (b) X-ray illumination image for simulation, (c) Image of model specimen (square opaque substance), (e) Projection image without noise, (f-1) Projection image with noise added ("Noise contrast"/"Contrast of diffraction fringes" $\simeq 1$), (f-2) Projection image with noise added ("Noise contrast"/"Contrast of diffraction fringes" $\simeq 0.95$), (g-1) and (g-2) Corrected images, (1) Noise removal and IFT, (2) Add target figure, (3) FT, (4) Add noise, (5) Iteration
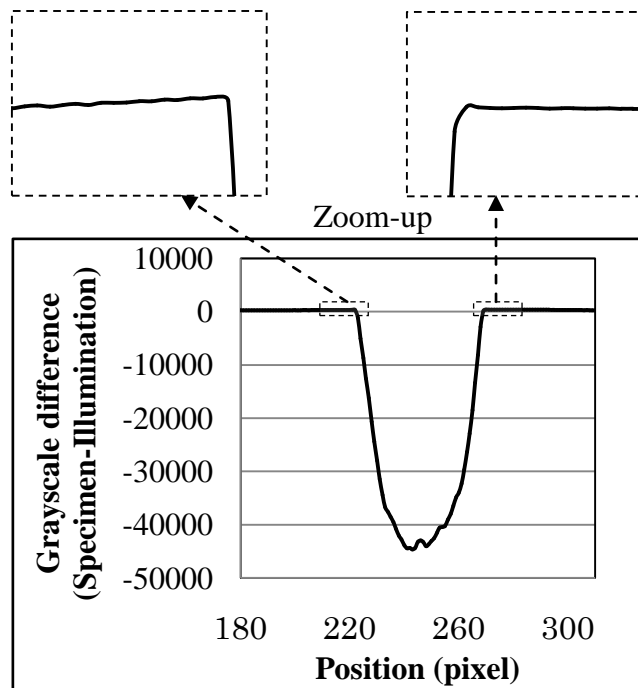
(A) "Noise contrast"/"Contrast of diffraction fringes" ≃0.95, Fig. 5.8 (g-1)
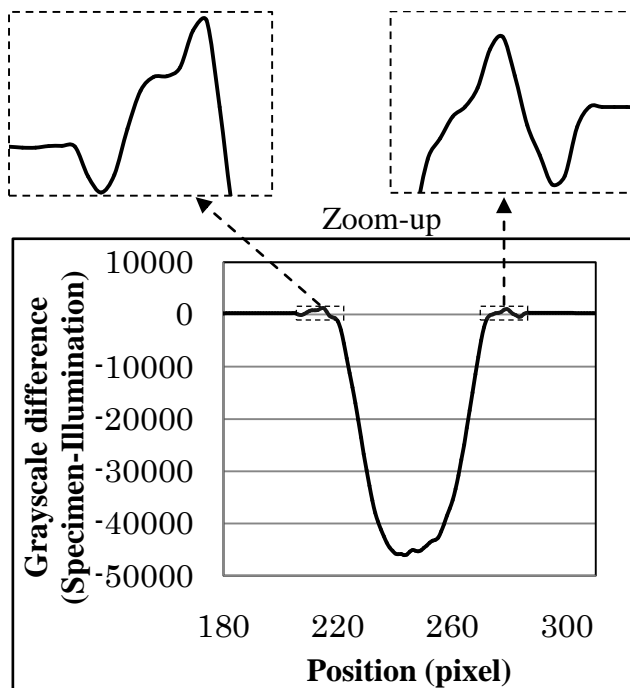
(B) "Noise contrast"/"Contrast of diffraction fringes" ≃1.00, Fig. 5.8 (g-2)

Fig. 5.9: Comparision of grayscale distributions on a cross-sectional line of correction images shown in Fig. 5.8 (g-1) and (g-2).

Thick line (▬): Corrected images (Fig.5.8 (g)), Thin line (—): X-ray illumination image (Fig.5.8 (b))

Fig. 5.10: Relationship between noise contrast of projection image and contrast of diffraction fringes in corrected image. (Simulation results for a chromosome image with relatively high contrast)

O and X: Correctable and uncorrectable regions for the ratio of the noise contrast to the contrast of the diffraction fringes, respectively.

(2) Iteration effect for the chromosome image with very low contrast:

The contrast for the target on the simulated projection image was adjusted to be same as that of an experimental projection image of chromosome with the magnification of 504 times, because the chromosome morphology was captured clearly on the image. The noise MSE was adjusted from 0 to $4*10^{6}$.

Relationship between contrast of target in the corrected image and noise MSE on the simulated projection image was examined for model specimens with small (0.7 μm * 0.7 μm) and big (1.4 μm * 1.4 μm) sizes. The specimen sizes were decided as the maximum and minimum when magnification of 500 times is required. The result is shown in Fig. 5.11. The horizontal axis is noise MSE on the simulated projection image and the vertical axis is the contrast of the target on the corrected image which was evaluated by equation (2) and normalized by the value for the noise MSE of 0. "O" and "X" characters show correctable and uncorrectable region of noise MSE, respectively (Our consideration for the judgment of correctable or uncorrectable region is explained in the second paragraph below).

Some representative images with noises of high and low noise MSE are shown in Fig. 5.12. The simulated projection images and their corrected images were shown in the left and the right side, respectively. An image of the model specimen prepared by simulation was also shown on the right side of the corrected images. The background noise on the simulated projection images was observable or unobservable for the image with high noise MSE ($4*10^6$) or with low noise MSE ($4*10^4$), respectively. For the corrected image with low noise MSE, traced line of the specimen boundary was equivalent to that of its projection images. It was also equivalent to the model specimen boundary. On the other hand, for the corrected image with high noise MSE, the contrast of the specimen image was lost by iteration procedure, resulting in inability to identify its morphology.

As shown in Figs. 5.11 and 5.12, the results were the same in the both cases of the specimen size. The image contrast decreased as the noise MSE became larger. The decreasing rate was slow until noise MSE reached about 10^5. The contrast decreased down to about 10%, and the decrease was not observable at the noise MSE less than 10^5. However, the decreasing rate became rapid when the noise MSE exceeded 10^5. Therefore, we concluded that the upper limit of the noise MSE where the image was corrected effectively by iteration procedure is 10^5 for the chromosome image. Since the noise MSE for an experimental projection image which was shown in Fig. 5.1 (a) was about 10^6, the result is consistent with our estimation as shown by the "A" character in Fig. 5.11.

Based on the evaluation obtained in this study, images should be captured with noises less than their upper limits after examining the noise on the image during experiments and optimizing the projection conditions. Moreover, development of new noise removal methods in image processing while keeping target morphology would be essential for better image correction.
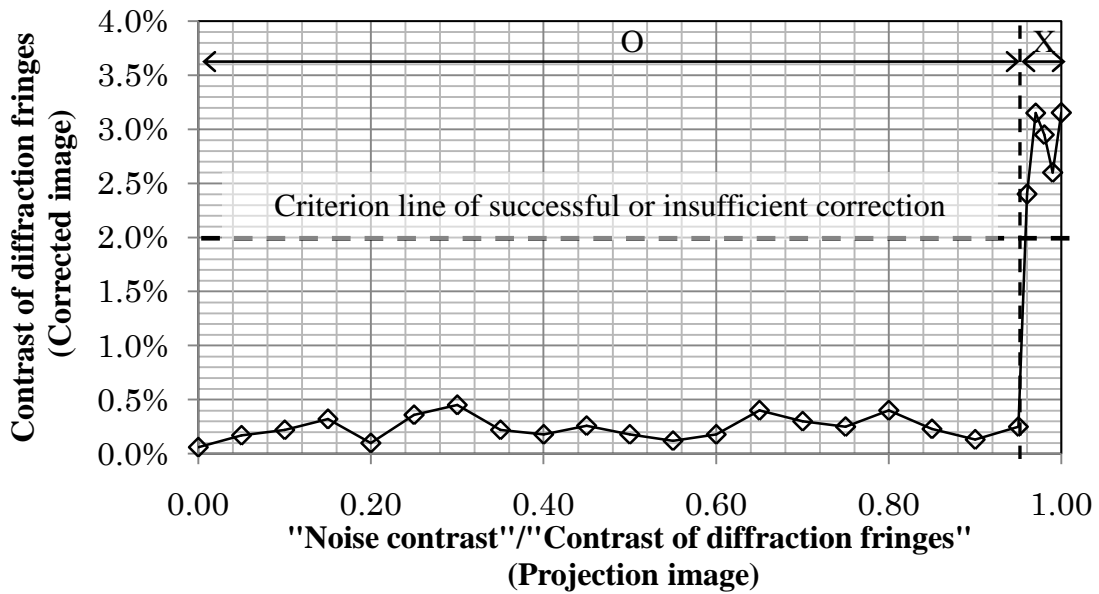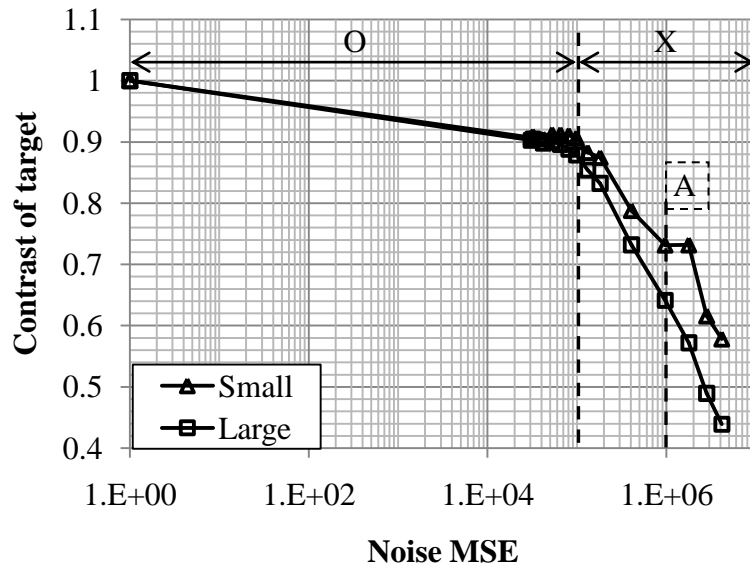
Fig. 5.11: Relationship between noise MSE of projection image and contrast of target in corrected image. (Simulation results for a chromosome image with very low contrast) O: Correctable region of the noise MSE, X: Uncorrectable region of the noise MSE, A: Noise MSE for the projection image of chromosome with the magnification of 504 times, Table 5.2
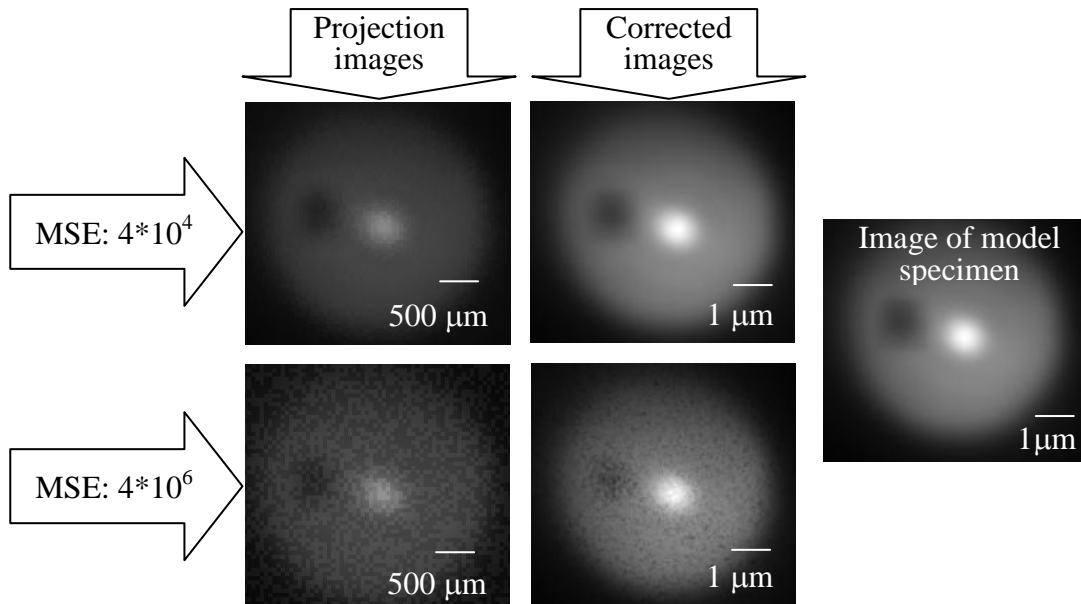

Fig. 5.12: Representative result of iteration effects on the projection images with very low contrast.

CHAPTER 6: CONCLUSION

In this study, we aimed at improving effectiveness of the iteration procedure and performed three steps of tests. In the first two steps, we applied projection images of two types of latex particles and chromosomes with magnification of 47 ~ 658 times to the iteration procedure, and evaluated the effectiveness of the iteration procedure and the effectiveness of an image improvement method prior to the iteration procedure. It was examined that the ineffective correction is mainly caused by high background noise on the projection image. Thus upper limit of the background noises on the projection image where the images were corrected effectively by the iteration procedure was evaluated as the third step.

Evaluation of the effectiveness of the iteration procedure was executed to consider the cause and the solutions of the ineffective correction. For the images of latex particles, iteration effect was good in the case of small size particle (diameter: 2 μm) or lower magnification (47 ~ 165 times). In contrast, the correction was not successful for those with larger size (diameter: 10 μm) and higher magnification (219 times or more). For the imaging of high magnification, the specimen is placed close to the point source of the soft X-ray. Therefore it was considered that majority of the illumination was shielded by the large latex particles, making the contrast of the diffraction fringe to decrease due to the decrease in the illumination intensity on the CCD screen. Thus, the contrast of the diffraction fringes was not identifiable by the iteration procedure.

All chromosome images were not correctable by the iteration procedure only. The reason was considered to be attributed to the decreased contrast of the diffraction fringes and specimen images due to the high transmittance of X-rays through the chromosome specimens and high background noise due to scattering from the specimen itself and debris of fragmented intracellular components of the specimen. For the corrected image with low magnifications (47 ~ 329 times), image contrast was relatively high and the diffraction fringes remained on the corrected image. The X-ray diffraction fringes were probably interrupted by the background noises, and resulted in inability to identify them solely by the iteration procedure.

For the corrected image with higher magnifications (504 ~ 658 times), the contrast of the specimen image was lost by the iteration procedure due to its extremely low contrast, resulting in the inability to identify its morphology.

Next we tried the individual and combined methods of contrast enhancement and noise removal prior to the iteration procedure (image improvement method). All images of latex particles and some images of chromosome with low magnification up to 329 times could be successfully corrected. However, the images with high magnification of 504 times or more were not correctable, yet. Therefore for the consideration of further improvement of the iteration procedure, we evaluated the upper limits of the noise where chromosome images could be corrected effectively by the iteration procedure by using a simulation study. As a result the upper limit of the noise MSE was determined as 10^5 which were 10 times lower than the noise MSE which was actually observed in the experiment.

In summary, we reached the following two achievements.

(1) The chromosome images with magnification of 47 ~ 329 times which were not correctable by the iteration procedure only could be corrected successfully by using an image improvement method consisting of a contrast enhancement and a noise removal methods prior to the iteration procedure.

(2) By using a simulation study, we evaluated an upper limit of the background noises on the images which is correctable by the iteration procedure with the image improvement. Also, the quantity of noise evaluation was decided. As a result, it became possible to examine the noise on projection images during experiments and to optimize the projection conditions by comparing the examination result to the upper limit of the noises.

The projection and correction methods are going to be developed further, especially for effective correction of the images with very low contrast.

Future problems to be addressed would be listed as follows:

(1) A simple and effective washing of the specimen using fresh fixative has been adopted to clean up the debris with few loss of the chromosomes. The effectiveness of washing specimens will be examined by in future studies.

(2) More noise removal methods of image processing are going to be investigated and the effectiveness of them will be compared for the better image correction.

BIBLIOGRAPHIES OR REFERENCES

[1] R. Weigert, N. Porat-Shliom and P. Amornphimoltham, Imaging Cell Biology in Live Animals: Ready for Prime time, *Journal of Cell Biology*, Vol. **201(7)**, 2013, pp. 969–979

[2] T. Paunesku, S. Vogt, T. C. Irving, B. Lai, R. A. Barrea, J. Master and G. E. Woloschak, Biological applications of X-ray microscopy, *International Journal of Radiation Biology*, Vol. **85**, Is. 8, 2009, pp. 710 - 713

[3] G. Schneider, B. Niemann, P. Gutmann, D. Weib, J.-G. Scharf, D. Rudolph and G. Schmahl, Visualization of 30 nm structures in frozen-hydrated biological samples by cryo transmission X-ray microscopy, *AIP Conference Proceeding*, Vol. **507**, 3, 2000

[4] R. Lewis, Medical applications of synchrotron radiation X-rays, Physics in Medicine and Biology, Vol. **42**, Num. 7, 1997, 1213

[5] S. Aoki, History and perspective of X-ray microscopes, *Optics*, Vol. **42**, Num. 6, 2013, pp. 280-288

[6] A. Ito and K. Shinohara, Soft X-ray microscopy and spectromicroscopy of cells, *Radioisotopes*, Vol. **47**, No. 10, 1998, pp. 789 - 798

[7] S. Aoki, III. Measurement by synchrotron radiation, 11. X-ray microscopy, *Radioisotopes*, Vol.47, No. 6, 1998, pp. 510 - 516

[8] J. Kirz, C. Jacobsen and M. Howells, Soft X-ray microscopes and their biological applications, *Quarterly Reviews of Biophysics*, Vol. **28**, 1995, pp. 33-130

[9] S. Williams, X. Zhang, C. Jacobsen, J. Kirz, S. Lindaas, J. Van't Hof and S. S. Lamm, Measurements of wet metaphase chromosomes in the scanning transmission X-ray microscope, *Journal of Microscopy*, Vol. **170** (Pt.2) , 1993, pp. 155-165

[10] K. Shinohara and A. Ito, Radiation damage in soft X-ray microscopy of live mammalian cells, *Journal of Microscopy*, Vol. **161** (Pt 3) , 1991, pp. 463-472

[11] E. F. Kaelble, eds.: Handbook of X-rays, McGraw-Hill, New York, 1967

[12] Y. Takeichi, N. Inami, H. Suga, T. Ueno, S. Kishimoto, Y. Takahashi and K. Ono, Development of a compact scanning transmission X-ray microscope, *Journal of Physics: Conference Series (IOP)*, Vol. **502**, 2014, 0112009

[13] G. McDermott, M. A. Le Gross and C. A. Larabell, Visualizing cell Architecture and molecule location using soft X-ray tomography and correlated cryo-light

microscopy, *Annual Review of Physical Chemistry*, Vol. **63**, 2012, pp. 225-239

[14] W. G. Müller, J. B. Heymann, K. Nagashima, P. Guttmann, S. Werner, S. Rehbein, G. Schneider, J. G. McNally, Towards an atlas of mammalian cell ultrastructure by cryo soft X-ray tomography, *Journal of Structural Biology*, Vol. **177**, 2012, pp. 179-192

[15] Y. Kinjo, K. Shinohara, A. Ito, H. Nakano, M. Watanabe, Y. Horiike, Y. Kikuchi, M. C. Richardson and K. A. Tanaka, Direct imaging in a water layer of human chromosome fibers composed of nucleosomes and their higher-order structures by laser-plasma X-ray contact microscopy, *Journal of Microscopy*, Vol. **176**, 1994, pp. 63–74

[16] K. Shinohara, H. Nakano, Y. Kinjo and M. Watanabe, Fine structure of unstained human chromosome fibres dried with no fixative as observed by X-ray contact, *Journal of Microscopy*, Vol. **158**, 1990, pp. 335-342

[17] J. Kirz and H. Rarback, Soft X-ray microscopes, *AIP Review of Scientific Instruments*, Vol. **56** Issue 1, 1985, pp. 1-13

[18] K. Shinohara, A. Ito, T. Honda, H. Yoshimura and K. Yada, Development of an X-ray projection microscope using synchrotron radiation, *AIP Conference Proceedings*, Vol. **507** Issue 1, 2000, pp. 346

[19] V. E. Cosslett and W. C. Nixon, X-ray shadow microscope, Nature, Vol. 168, 1951, pp. 24-25

[20] K. Yada and S. Takahashi, Projection X-ray microscope observation of biological samples, X-ray Microscopy in Biology and Medicine, Japan Science Society Press, Tokyo/Springer-Verlag, Berlin, 1990, pp. 203-212

[21] T. Shiina, T. Suzuki, T. Honda, A. Ito, Y. Kinjo, H. Yoshimura, K. Yada and K. Shinohara, Fresnel diffraction correction by phase-considered iteration procedure in soft X-ray projection microscopy, *Journal of Physics: Conference Series (IOP)*, Vol. **186**, 2009, pp. 12059-1-12059-3

[22] S. C. Chikwendu, Non-linear wave propagation solutions by Fourier transform perturbation, *Int. J. Non-linear Mechanics*, Vol. **16**, 1981, pp. 117-128

[23] J. W. Cooley and J. W. Turkey, An algorithm for the machine calculation of complex Fourier series, *Mathematics of Computation*, Vol. **19**, No. 90, 1965, pp. 297-301

[24] J. M. Robertson, X-ray analysis and application of Fourier series methods to molecular structure, *Reports on Progress in Physic*s, Vol. **4**, 1937, pp. 332-367

[25] P. J. Nahin, Oliver Heaviside, the John Hopkins University press, Baltimore and London, 2002

[26] A. V. Durrant, Vectors in physics and engineering, Chapman and Hall, London, 1996

[27] S. Mobilio and F. Boscherini, Synchrotron radiation: Basics, methods and applications, Springer- Verlag Berlin Heidelberg, 2015

[28] E.E. Koch, D.E. Eastman and Y. Farges, Handbook of synchrotron radiation, North-Holland Publishing Company, Amsterdam, 1983

[29] H. Onuki and P. Elleaume, Wigglers, undulators and their applications, Taylor and Francis, New York, 2004

[30] M. Akul, Introduction to the electromagnetic spectrum and spectroscopy, *Analytical Chemistry Notes*, 2011

[31] S. Eidelman *et al.* [Particle Data Group], Review of particle physics, *Physics Letters B*, Vol. **592**, 2004

[32] M. Born and E. Wolf, Principles of optics, Cambridge University Press, 1999

[33] O. K. Ersoy, Diffraction, Fourier optics and imaging, John Wiley and Sons, Inc, Hoboken, New Jersey, 2007

[34] J. W. Goodman, Introduction to Fourier optics, third edition, Roberts and company, Englewood, Colorado, 2005

[35] Grant R.Fowles, Introduction to modern optics, Dover Publication INC., New York, 1989

[36] Outline of the accelerators, *PF Activity Report 2010*, Vol. **28**, 2011, pp. 111-113

[37] PF home page (beamlines and experimental stations):
http://www2.kek.jp/imss/pf/apparatus/bl/

[38] S. Asaoka et al., New upgrade project for the Photon Factory Storage ring, *AIP Conference Proceedings*, Vol. **705**, 2004, pp. 161

[39] PF Home page (BL-11A Soft X-ray Grazing Incidence Monochromator Station):
http://pfwww.kek.jp/sxspec/sx/bl11a/40223.html

[40] S. Y. Lee, Accelerator Physics, second edition, World Scientific Publishing, Singapore, 2004

[41] B. Rautenstrauß and T. Liehr (eds.), FISH technology, Springer lab manual, Springer Verlag Berlin Heidelberg, 2002, pp.73-81

[42] C. F. Bohren and E. E. Clothiaux, Fundamentals of atmospheric radiation, Wiley-VCH Verlag GmbH & Co. KGaA, Fedral Republic of Germany, 2006

[43] S. S. Al-amri, N. V. Kalyankar and S. D. Khamitkar, Linear and non-linear contrast enhancement image, *IJCSNS International Journal of Computer Science and Network Security*, Vol. **10**, No.2, 2010, pp. 139-143

[44] G. A. Baxes, Digital image processing: Principles & applications, Wiley & Sons,

Inc.: New York, 1994

[45] D. Salomon, Data compression: The complete reference, fourth edition, Springer-Verlag London Limited, 2007

[46] C. G. Rafael, E. W. Richard, Digital image processing, Addison-Wesley, New York, 1992

[47] E. Peli, Contrast in complex images, *Journal of the Optical Society of America A*, Vol. **7**, No. 10, 1990, pp. 2032-2040